

Dr Bidlot

Thank you for your comments, to which we hope our responses and subsequent changes in the manuscript adequately address.

p10, line 24: Charnock is not constant because it is sea state dependent. Bidlot et al. 2014 show a nice example, where a wave model was used to calculate Charnock, including areas with sea ice. In that paper, the drag experienced by the atmosphere was shown for all wind conditions for both Arctic and Antarctic combined. For small ice fractions,  $C_d$  varies by almost one order of magnitude with a median value of  $1.5 \cdot 10^{-3}$ . The mean Charnock was around 0.01 for winds below 5m/s and 0.03 for wind above 18m/s with a linear to quadratic growth in between (Bidlot private communication).

We agree that the constant seems to be the Charnock 'constant' is not actually a constant, but is related in some way to the wave field, although the details are still under debate. In any case, in our case studies the flow was always off the ice edge, so wave development was minimal. Consequently waves are not significantly affecting our results.

P15, line 22: COARE 4 is a better reference Edson, J., V. Jampana, R. Weller, S. P. Bigorre, A. J. Plueddemann, C. W. Fairall, S. D. Miller, L. Mahrt, D. Vickers, and H. Hersbach (2013), On the exchange of momentum over the open ocean, *J. Phys. Oceanogr.*, 43, 1589–1610, doi:10.1175/JPO-D-12-0173.1.

For logistical reasons, we used COARE version 3 rather than 4. Since the use of COARE here is not a particularly important part of the paper, we don't believe this is worth changing.

Would it have been possible to analyse the data to also present a parameterisation for  $z_0$  in terms of sea ice cover as presented for ECMWF. Weather models tend to represent the surface properties in terms of roughness length scale.

We agree, and have added a new plot (Fig. 10b) showing effective  $z_0$  against sea ice concentration, with effective  $z_0$  derived from effective  $CDN_{10}$  (as shown now in Fig. 10a).

## C. Lüpkes

This paper presents atmospheric drag coefficients over fractional sea ice cover derived from measurements with two aircraft over the Fram Strait and Barents Sea. These drag coefficients are compared with results of the most recent parameterizations which calculate drag coefficients as the sum of skin drag coefficients over open water and sea ice and of a form drag coefficient describing the drag caused by ice floe edges. The main findings are that the observations agree well with results obtained from our parameterization (Lüpkes et al., 2012) (L2012) although complex conditions with variable sea ice morphology have been considered. Finally, improvements are proposed for open constants in the parameterization.

The authors mention that such new observations are urgently needed since the majority of measurements has been carried out 20 years ago and thus before the current larger change of Arctic sea ice.

I fully agree with this point. Furthermore, in my opinion this paper is excellently written, very clearly organized and I think that the data help a lot to understand strengths and weaknesses of the considered parameterizations. As the authors write, it is the largest set of aircraft observed data of this kind. I am impressed also by the degree of agreement with the parameterization by L2012. I have only minor revisions and recommendations which might help to once more improve a little the current version of the manuscript.

Thank you for your consideration and praise of our paper. We have made changes according to your comments and believe the paper to have been improved as a result.

### Minor Revisions

1. page 26618, lines 3-5: When we called  $C_{dn10;i}$  skin drag we were aware of the fact that this 'skin drag' consists again of a sum of 'real' skin drag (drag over a smooth ice surface) and of form drag by ridges. This form drag can be calculated with a similar concept (see Andreas, 2011; Garbrecht et al., 2002). The latter citations could be added here.

Thanks for drawing our attention to these studies. We have added a sentence citing these studies (final sentence of Section 4).

2. page 26623 line 25; page 26624 line 1; page 26629 line 10: Similar point as above. Castellani et al. (2014) document the variability of drag coefficients based on Arctic wide observations of topography (sea ice morphology). This could be mentioned here.

Thanks, this is a relevant paper, and provides an independent check (via a different methodology) of drag coefficients to the other airborne studies we discuss in the introduction. A sentence has been added citing this paper in the introduction.

3. page 26621, line 25 and 26622 line 1: Due to our experience the assumption of a constant flux layer leads to an underestimation of neutral 10 m drag coefficients when they are derived from aircraft measurements in 40 m height in neutral or stable conditions. This is the reason why in Garbrecht et al. (2002) (their figure 9) another procedure has been used. It is unclear, however, up to now what happens under unstable conditions. So, I suggest adding here in addition to your references just that the assumption of a constant flux layer is the best what can be done at present but this could be an issue for future research. (see also next item). Addition of mixed layer heights  $z_i$  (if available) would be useful since the accuracy of the constant flux layer assumption depends on  $z_i$ .

A sentence has been added along the lines of that suggested

4. page 26627, line 15: I agree, the value of  $c_e$  can be tuned. But with respect to the previous point (constant flux layer assumption) I would not exclude that the 'measured' drag coefficients are slightly underestimated. This point could be mentioned as a possible uncertainty of the new recommended value.

Whilst we agree that there is a case to be made for a slight underestimate in our drag values due to the constant flux layer assumption, as you highlight this error cannot easily be characterised or quantified, and it may be masked by other similarly small systematic errors in our methodology. In the aid of keeping interpretation of the paper simple, we don't think mentioning this point is necessary. We have discussed the quality control procedure and the assumptions we have made in our methodology.

5. page 26628, line 2: L2012 propose to use Charnock for  $z_{0;w}$  (equation 14). How does this agree with your measurements?

Charnock-derived  $z_{0;w}$  compares well with our observed values – supporting the proposition of L2012. Note that we do mention in the paper that our observations over open water show good agreement with the COARE algorithm:

Page 26623, lines 19-22: "Our bin-averaged CDN10 values over open sea water compare well with those expected by inputting observed wind speeds into the well-established COARE bulk flux algorithm of Fairall et al. (2003). Values derived from COARE Version 3.0 consistently lie within the interquartile range."

6. page 26629, line 17-22: One could discuss this mentioning equation 11 and its dependence on the aspect ratio  $h_f/D_i$ . Small  $D_i$  and large  $h_f$  will increase  $C_d$ . The sensitivity has been discussed by Lüpkes and Birnbaum (2005) (their Figure 7).

Reference has now been made to Equation 11 in this sentence.

7. page 26630, line 18: One could add that 5  $\text{ms}^{-1}$  is a value that is typical for Arctic summer.

It is now mentioned that our observed mean winds are close to the climatological mean.

8. e.g. page 26634, line 25: Lüpkes and Gryanik (2015) show that the peak value for the surface drag is also a function of stratification. A future challenge is also to validate and quantify this finding.

A sentence noting that peak surface drag is a function of sea ice morphology and stratification (referencing this work) has been added.

9. The L2012 scheme is available in different stages of complexity. The most simple one was considered in Lüpkes et al. (2013) and it was called there AWI parameterization with three different parameter sets (AWI, AWI+ and AWI-) giving the range of possible variability. In this scheme  $C_d$  is just a function of the sea ice concentration. This could be considered in addition here or in another work.

Yes, the fact that we only consider here the simplest version of the L2012 scheme is implied in our Section 2.3 and in the conclusions ("Our results suggest that the simplification of the L2012 scheme

by parameterizing floe dimension ( $D_i$ ) and freeboard ( $h_f$ ) in its expression for form drag on floe edges using  $A$  provides sufficiently accurate results.”). Unfortunately our observations did not include measurements of ice morphology parameters  $h_f$  or  $D_i$ , and so we were unable to compare these levels of complexity. Regardless, we find that the most simple version compares well with our observations, so long as the background ice roughness is accounted for (i.e. CDN at  $A=1$  is anchored to the observations).

## References

Andreas, E.L (2011), A relationship between the aerodynamic and physical roughness of winter sea ice, Q. J. R. Meteorol. Soc., 137, 927-943.

Castellani, G., C. Lüpkes, S. Hendricks, and R. Gerdes (2014), Variability of Arctic sea-ice topography and its impact on the atmospheric surface drag, J. Geophys. Res. Oceans, 119(10), 6743-6762, doi:10.1002/2013JC009712.

Garbrecht, T., C. Lüpkes, J. Hartmann, and M. Wolff (2002), Atmospheric drag coefficients over sea ice-validation of a parametrisation concept, Tellus A, 54(2), 205-219.

Other references are given in the manuscript.

**T. Vihma**

The manuscript is based on a large amount of data and the analyses are well planned, detailed, and carefully made. The manuscript is well written. I suggest acceptance subject to minor revisions specified below.

Thank you for your positive comments on our paper, and insightful suggestions.

1. The first sentence of the Introduction is an oversimplification. In addition to the three forces mentioned, sea ice motion is affected by the sea surface tilt and Coriolis force (e.g. Vihma and Launiainen (1993), JGR, equation (1), but be aware of the missing + sign between ice-water stress and internal stress). The Coriolis force affects the deviation angle between the wind and ice drift vectors (also affected by the internal ice resistance and ice-water drag). The thicker is the ice, the larger is the deviation angle due to Coriolis force.

Noted, and text changed to include the additional forces. First sentence now reads "Sea ice movement is determined by five separate forces: a drag force from the atmosphere, a drag force from the ocean, internal sea-ice stresses, a downhill ocean-surface slope force, and the Coriolis force (e.g. Notz 2012)."

2. The importance of the results could be better illustrated via idealized calculations. For example, to illustrate the importance of the differences between the drag coefficients obtained from different parameterizations, you could calculate their effect on 10-m wind speed, assuming neutral stratification and a certain wind speed above the boundary layer. Further, the sensitivity of the ice drift speed on the value of the drag coefficient could be calculated assuming a certain 10-m wind speed, steady-state conditions, no ocean current, and a certain value for the ice-water drag coefficient. Some more assumptions / idealizations may be needed. Such calculations would help a non-specialist to understand how much a small difference in the drag coefficient matters for the dynamics of the atmosphere and sea ice.

Whilst we agree that the above would be an interesting exercise, we don't think it belongs in this paper, where the purpose is to present our results based on our observations and assess the performance of parameterization schemes against these observations. Note that the recent publication by Lupkes et al. (2013) starts on such an exercise. This would certainly be something for the future.

**Observations of surface momentum exchange over the marginal-ice-zone and  
recommendations for its parameterization**

Andrew D. Elvidge<sup>1\*</sup>, Ian A. Renfrew<sup>1</sup>, Alexandra I. Weiss<sup>2</sup>,  
Ian M. Brooks<sup>3</sup>, Tom A. Lachlan-Cope<sup>2</sup>, John C. King<sup>2</sup>

<sup>1</sup>*School of Environmental Sciences, University of East Anglia, Norwich, UK*

<sup>2</sup>*British Antarctic Survey, Cambridge, UK*

<sup>3</sup>*School of Earth and Environment, University of Leeds, Leeds, UK*

\*Correspondence to: Dr A. D. Elvidge, Centre for Ocean and Atmospheric Sciences, School of  
Environmental Sciences, University of East Anglia, Norwich, UK. E-mail: a.elvidge@uea.ac.uk

Atmospheric Chemistry and Physics

First submission: 14 August, 2015

## Abstract

Comprehensive aircraft observations are used to characterise surface roughness over the Arctic marginal ice zone (MIZ) and consequently make recommendations for the parameterization of surface momentum exchange in the MIZ. These observations were gathered in the Barents Sea and Fram Strait from two aircraft as part of the Aerosol–Cloud Coupling And Climate Interactions in the Arctic (ACCACIA) project. They represent a doubling of the total number of such aircraft observations currently available over the Arctic MIZ. The eddy covariance method is used to derive estimates of the 10-m neutral drag coefficient ( $C_{DN10}$ ) from turbulent wind velocity measurements, and a novel method using albedo and surface temperature is employed to derive ice fraction. Peak surface roughness is found at ice fractions in the range 0.6 to 0.8 (with a mean interquartile range in  $C_{DN10}$  of  $1.25$  to  $2.85 \times 10^{-3}$ ).  $C_{DN10}$  as a function of ice fraction is found to be well approximated by the negatively skewed distribution provided by a leading parameterization scheme (Lüpkes et al., 2012) tailored for sea ice drag over the MIZ in which the two constituent components of drag – skin and form drag – are separately quantified. Current parameterization schemes used in the weather and climate models are compared with our results and the majority are found to be physically unjustified and unrepresentative. The Lüpkes et al. (2012) scheme is recommended in a computationally simple form, with adjusted parameter settings. A good agreement ~~is found to hold~~ for subsets of the data from different locations, despite differences in sea ice conditions. Ice conditions in the Barents Sea, characterised by small, unconsolidated ice floes, are found to be associated with higher  $C_{DN10}$  values – especially at the higher ice fractions – than those of Fram Strait, where typically larger, smoother floes are observed. Consequently, the important influence of sea ice morphology and floe size on surface roughness is recognised, and improvement in the representation of this in parameterization schemes is suggested for future study.

## 1. Introduction

Sea ice movement is determined by ~~three-five~~ separate forces: a drag force from the atmosphere, a drag force from the ocean ~~and~~, internal sea-ice stresses, a downhill ocean-surface slope force, and the Coriolis force (e.g. Notz 2012). The two drag forces are associated with a surface exchange of momentum across the atmosphere-ice or the ice-ocean boundary respectively. These exchanges impact the dynamical evolution of both atmosphere and ocean; here we focus on the interaction with the atmosphere only. Within the atmospheric surface layer (where the turbulent stress remains close to its surface value) the wind speed,  $U(z)$ , is related to the surface stress through:

$$U = \frac{u_*}{\kappa} \left[ \ln \left( \frac{z}{z_0} \right) - \varphi \right], \quad (1)$$

where  $\mathbf{u}_*$  is the friction velocity,  $\kappa$  is the von Karman constant (0.4),  $z_0$  is the roughness length for velocity and  $\varphi$  is a stratification correction function (see, for example, Stull (1988) for further details about this similarity theory approach). The aerodynamic roughness length,  $z_0$ , describes the level at which the wind speed described by Eq. (1) becomes zero and represents the physical roughness of the surface (Stull 1988). The momentum exchange (or surface stress) is then:

$$\tau = \rho \mathbf{u}_*^2 = \rho C_D U^2, \quad (2)$$

where  $\rho$  is the density and  $C_D$  is the drag coefficient for the fluid at height  $z$ . Combining equations (1) and (2) we can directly relate the drag coefficient and roughness length; for example, for neutrally stratified conditions and  $z = 10$  m:

$$C_{DN10} = \left( \frac{u_*}{U_{10N}} \right)^2 = \frac{\kappa^2}{\ln(10/z_0)^2}. \quad (3)$$

Over a rough surface the drag has two components: a surface skin drag caused by friction and a form drag caused by pressure forces from the moving fluid impacting on roughness elements (Arya 1973, 1975). The form drag acts on sea-ice ridges, on floe edges, on melt pond edges and on surface undulations of all types. In other words, it is a function of the morphology of the sea ice and consequently it is strongly related to ice concentration and thickness.

To parameterize surface drag in numerical weather prediction, climate or earth system models the above formulae are implemented to determine the surface stress for a given fluid velocity and stability<sup>1</sup>. To do this  $C_D$ , or equivalently  $z_0$ , must be prescribed and so observations of these parameters for different sea-ice surfaces are required. To calculate these for the atmosphere-ice boundary, for example, observations of surface-layer momentum flux, wind speed and atmospheric stability are required. These are challenging observations to make over sea ice and even more challenging over the marginal-ice-zone (MIZ).

Over the main sea-ice pack, with ice fraction,  $A$ , close to 1, early studies based on tower or aircraft observations of turbulent fluxes estimated  $C_{DN10}$  as ranging from  $\sim 1\text{--}4 \times 10^{-3}$  for continuous sea ice, depending on the ice morphology. In a comprehensive review, Overland (1985) breaks down this range by morphology and location: for large flat floes  $C_{DN10}$  ranges from  $1.2\text{--}1.9 \times 10^{-3}$  and a median of  $1.5 \times 10^{-3}$  is given (e.g. based on Banke and Smith (1971) over the Canadian Arctic); for rough ice with pressure ridges  $C_{DN10}$  ranges from  $1.7\text{--}3.7 \times 10^{-3}$ ; over first year ice in Marginal Seas (e.g. the Beaufort Sea or Gulf of St Lawrence) the  $C_{DN10}$  subjective median values are from  $2.2\text{--}3.0 \times 10^{-3}$ . [More recently, Castellani et al. \(2014\) use airborne-derived laser altimeter data gathered between 1995 and 2011 in conjunction with a sea ice drag parameterization scheme to](#)

<sup>1</sup> Note a turning angle between the fluid and the ice surface is also required if the surface-layer Ekman spiral is not resolved (Notz 2012; Tsamados et al. 2014).



demonstrate the considerable topographic and geographic variability in  $C_{DN10}$  over Arctic pack ice, with values ranging between  $1.5$  and  $3 \times 10^{-3}$ , largely corroborating the results of earlier studies.;

For the MIZ, data is not so readily available. On the “inner MIZ”, with ice fractions of  $0.8$ - $0.9$  and consisting of small and rafted floes, Overland (1985) report there are only a few data sets, available with  $C_{DN10}$  ranging from  $2.6$ - $3.7 \times 10^{-3}$ ; while for the “outer MIZ”, with  $A = 0.3$ - $0.4$ , the only two values provided are  $C_{DN10} = 2.2$  and  $2.8 \times 10^{-3}$  from MIZEX-1984 over the Greenland Sea (Overland 1985) and from the Antarctic MIZ using an indirect balance method (Andreas et al. 1984). Further drag measurements over the MIZ using aircraft were made by Hartman et al (1994) and Mai et al. (1996) as part of the ‘REFLEX’ and ‘REFLEX II’ experiments over Fram Strait. Hartman et al. (1994) obtained 16  $C_{DN10}$  values with ranges of  $C_{DN10} = 1.0$ - $2.3 \times 10^{-3}$  for  $A = 0.5$ - $0.8$  and  $C_{DN10} = 1.1$ - $1.6 \times 10^{-3}$  for  $A = 0.9$ - $1.0$ . They found generally higher  $C_{DN10}$  values over ice fractions of  $0.5$ - $0.8$ . Mai et al. (1996) found a similar range over their 85 12-km runs, with  $C_{DN}$  ranging from  $\sim 1.3 \times 10^{-3}$  over open water, to a maximum of  $\sim 2.6 \times 10^{-3}$  at  $A = 0.5$ - $0.6$ , then decreasing to about  $1.8 \times 10^{-3}$  for  $A = 1$ . Schröder et al. (2003) largely corroborate these results with their 32 runs, finding a mean  $C_{DN10}$  of  $2.6 \times 10^{-3}$  for  $A = 0.5$  over Fram Strait and a mean  $C_{DN10}$  of  $1.6 \times 10^{-3}$  for  $A = 0.86$  over the Baltic Sea. These aircraft-based MIZ drag results are compiled together in Lüpkes and Birnbaum (2005). In short, they suggest that  $C_{DN10}$  peaks over the MIZ ( $A \approx 0.5$ - $0.6$ ) and decreases for lower or higher ice fractions.

Reviewing the above, however, it is clear that further surface drag measurements over the marginal-ice-zone are critical for validating and developing parameterizations of surface exchange over sea ice. At present there are only about 150 individual data points for the MIZ from aircraft observations in the literature and the majority of these are from the same research group and platform. The majority were also made more than twenty years ago and, as has been well-documented, Arctic sea ice is changing in extent and characteristics (e.g. Kwok and Rothrock 2009; Markus et al. 2009). It is clear that new additional observations are urgently required. Improvements to the representation of sea-ice are planned for many global weather forecasting models in order to aid both seasonal forecasting and shorter-term forecasting for the polar regions (e.g. ECMWF 2013). These models typically have grid sizes of  $10$ - $25$  km, meaning they will have the resolution to represent gradients in ice fraction across the MIZ and therefore need to parameterize MIZ interactions with the atmosphere. In addition, higher-resolution regional coupled atmosphere-ocean-ice models are providing improved skill and starting to be used operationally (Pellerin et al. 2004; Smith et al. 2013); while climate and earth system models are also increasing in resolution and these will all require accurate surface exchange over the MIZ. Recent ocean-ice and atmosphere-ocean-ice modelling studies have demonstrated considerable sensitivity to surface exchange parameterization over sea ice, particularly in their simulations of sea-ice thickness and

118 extent (Tsamados et al. 2014; Rae et al. 2014) and the polar ocean (Stössel et al. 2008; Roy et al.  
 119 2015). Simulations of the near-surface atmosphere can also be significantly affected (Rae et al.  
 120 2014).

121 Here we present over 200 new estimates of surface drag over the MIZ in Fram Strait and the  
 122 Barents Sea from two independent research aircraft. This represents a more than doubling of the  
 123  $C_{DN}$  estimates currently available for surface exchange parameterisation development. Only low-  
 124 level legs (mainly 30-40 m above sea level) are used to provide quality-controlled eddy-covariance  
 125 estimates of the turbulent momentum flux. We use this data to provide a validation of the leading  
 126 parameterization schemes and make recommendations for parameter settings. In the next section we  
 127 present a brief review of surface exchange parameterizations. Section 3 covers data and methods  
 128 and Section 4 presents our results. In Section 5 recommendations for the parameterization of drag in  
 129 the MIZ are made, before our conclusions in Section 6. [Note a summary of variable notation is](#)  
 130 [provided at the end of the paper.](#)

## 132 2. Parameterizing surface momentum exchange over sea ice

### 133 2.1 Background

134 All atmospheric models require an exchange of momentum with the surface for accurate  
 135 simulations. Over sea ice this has generally been treated rather crudely, usually with a constant drag  
 136 coefficient prescribed for all sea-ice types and thicknesses (e.g. Notz 2012; Lüpkes et al. 2013). For  
 137 model grid boxes that are partially ice-covered a ‘mosaic method’ is commonly employed, which  
 138 typically calculates the flux over the ice and water surfaces separately, then averages these in  
 139 proportion to the surface areas (e.g. Claussen 1990; Vihma 1995). Unfortunately using this  
 140 approach with a constant drag coefficient does *not* represent momentum exchange over the MIZ  
 141 correctly. It results in a linear function of  $C_{DN}$  with  $A$  rather than the maximum in drag at  
 142 intermediate ice concentrations supported by observations.

143 Both empirical and physical-based parameterizations of surface drag have recently been  
 144 developed. Andreas et al. (2010) composited together all available MIZ  $C_{DN}$  observations (primarily  
 145 from Hartmann et al. 1994 and Mai et al. 1996) with the vast number of summertime sea-ice pack  
 146  $C_{DN}$  observations from the SHEBA project (Uttal et al. 2002) for  $A > 0.7$ . They argued that  
 147 summertime sea-ice, replete with melt ponds and leads, was morphologically similar to the MIZ and  
 148 so these data sets could be combined. Plotting  $C_{DN}$  against  $A$ , and ignoring various outliers, they  
 149 found a maximum in  $C_{DN}$  around  $A = 0.6$ . They empirically fitted by eye a second order polynomial  
 150 to this data set:

$$151 \quad 10^3 C_{DN} = 1.5 + 2.233A - 2.333A^2. \quad (4)$$

Here,  $C_{DN}$  is simply a function of ice fraction ( $A$ ), and other morphological characteristics are neglected.

A series of physical-based parameterization schemes for surface drag has also been developed based on trying to capture the effect of form drag by equating sea-ice characteristics to roughness elements. The form drag is added to the skin drag to give a total surface drag, as represented in these schemes by:

$$C_{DN} = (1 - A)C_{DNw} + AC_{DNI} + C_{DNf}, \quad (5)$$

where  $C_{DNw}$  and  $C_{DNI}$  are the neutral skin drag coefficients over open water and continuous ice respectively, and  $C_{DNf}$  is the neutral form drag coefficient. This approach has its basis in work by Arya (1973, 1975) that has been developed and refined – see Hanssen-Bauer and Gjessing (1988), Garbrecht et al. (1999, 2002), Birnbaum and Lüpkes (2002), Lüpkes and Birnbaum (2005), Lüpkes et al. (2012), and Lüpkes and Gryanik (2015).

Amongst the leading MIZ drag schemes currently being implemented is that set out in Lüpkes et al. (2012; referred to hereafter as L2012). This scheme has been adapted for use in the Los Alamos sea ice model CICE (Tsamados et al., 2014; Hunke et al. 2015). It determines neutral 10-m drag coefficients ( $C_{DN10}$ ) over 3-dimensional ice floes as a function of sea ice morphological parameters: sea ice fraction as a minimum and, optionally, freeboard height and floe size. Lüpkes et al. (2013) illustrate the substantial impact such a parameterization has on  $C_{DN}$  for summertime Arctic sea ice in contrast to the constant exchange coefficient approach that is currently standard in climate models.

## 2.2 Derivation of form drag

As a result of its sensitivity to sea ice morphology, representing the form drag component of  $C_{DN}$  in a parameterization scheme is a complex procedure. Its derivation in the L2012 scheme is best approached by considering a domain, of area  $S_t$ , containing  $N$  identical ice floes of cross-wind length  $D_i$  and freeboard height  $h_f$ . If the area fraction of ice within the domain is given by  $A$ ,

$$S_t = c_s \frac{N D_i^2}{A}, \quad (6)$$

where  $c_s$  relates the deviation of the mean floe area from that of a square (so that  $c_s = 1$  for a square and, for example,  $c_s = \frac{\pi r^2}{4r^2} = \frac{\pi}{4}$  for a circle). The total form drag acting on the frontal areas of ice floes within the domain is provided by

$$f_d = N c_w S_c^2 D_i \int_{z_{0w}}^{h_f} \frac{\rho [U(z)]^2}{2} dz. \quad (7)$$

Here,  $c_w$  is the fraction of the available force which effectively acts on each floe (Garbrecht et al., 1999);  $S_c$  is the sheltering function, which tends towards 0 for small distances between floes

(implying a large sheltering effect) and tends towards 1 for large distances;  $z_{0w}$  is the mean local roughness length over open water; and  $U(z)$  is the upstream wind speed. Recall from equation (1)  $U(z)$  increases logarithmically with height, so the 10-m neutral wind speed is

$$U_{N10} = (u_*/\kappa) \ln(10/z_{0w}) . \quad (8)$$

Noting that the surface wind stress due to form drag is simply the frontal force per unit area  $\tau_d = f_d/S_t$ ,  $C_{DNf}$  can be evaluated at the 10 m height according to equations (3) and (8) as follows:

$$C_{DN10f} = \frac{\tau_d}{\rho U_{N10}^2} = \frac{f_d / S_t}{\rho (u_*/\kappa)^2 \ln^2(10/z_{0w})} . \quad (9)$$

Equations (6) and (7) are inserted into (9), and the integral in (7) is solved with the aid of (8) to yield

$$C_{DN10f} = A \frac{h_f}{D_i} S_c^2 \frac{c_e}{2} \left[ \frac{[\ln(h_f/z_{0w}) - 1]^2 + 1 - 2 z_{0w}/h_f}{\ln^2(10/z_{0w})} \right] , \quad (10)$$

where the effective resistance coefficient  $c_e = c_w/c_s$ . Finally, following the removal of insignificant terms in the above (resulting in a deviation typically less than 1% according to L2012), we obtain

$$C_{DN10f} = A \frac{h_f}{D_i} S_c^2 \frac{c_e}{2} \left[ \frac{\ln^2(h_f/z_{0w})}{\ln^2(10/z_{0w})} \right] . \quad (11)$$

### 2.3 The L2012 parameterization: equation summary

The overall drag coefficient is the sum of the skin and form drag components, so substituting (11) into equation (5):

$$C_{DN10} = (1 - A)C_{DN10w} + AC_{DN10i} + A \frac{h_f}{D_i} S_c^2 \frac{c_e}{2} \left[ \frac{\ln^2(h_f/z_{0w})}{\ln^2(10/z_{0w})} \right] . \quad (12)$$

Note our equations (11) and (12) are identical to L2012 equations (51) and (22). L2012 defines  $C_{DN10w}$  and  $C_{DN10i}$  as skin drag terms. However, this assumes there is no form drag over open water or continuous sea ice, since the form drag contribution given by Equation 11 only accounts for form drag on ice floe edges. In reality, additional form drag can be produced in the ocean due to waves, and over ice due to ridging and other roughness features caused by deformation and melt. Consequently,  $C_{DN10w}$  and  $C_{DN10i}$  are better expressed as the total (skin *and* form) drag over open water and continuous sea ice, respectively. The former is provided by

$$C_{DN10w} = \kappa^2 \ln^{-2}(10/z_{0w}) , \quad (13)$$

using equation (3). Note that  $z_{0w}$  is usually provided in models as a function of the surface stress on the sea surface and the gravitational restoring force via a modified Charnock relation

$$z_{0w} = \alpha \frac{u_*^2}{g} + b \frac{\nu}{u_*} , \quad (14)$$

where  $\alpha$  is the Charnock constant,  $b$  is the smooth flow constant and  $\nu$  is the dynamic viscosity of air (e.g. Fairall et al. 2003). L2012 set  $\alpha = 0.018$  and  $b = 0$ . It is more common to include the

smooth flow term, usually with  $b = 0.11$ , so that there is some momentum exchange at low wind speeds (e.g. Renfrew et al. 2002; Fairall et al. 2003). The first term leads to an increase in roughness, and hence drag coefficient, as the wind speed increases. This increase is related to wave-induced roughness and is now reasonably well-constrained for low to moderate wind speeds, but there is some uncertainty at higher wind speeds (Fairall et al. 2003; Petersen and Renfrew 2009; Cook and Renfrew 2015). Various values for the Charnock ‘constant’ are used, typically between 0.011 and 0.018. In the Fairall et al. (2003) review they suggest  $\alpha$  should linearly increase from 0.011 to 0.018 (between  $U_{N10} = 10$ -18 m s<sup>-1</sup>), although they note some uncertainty in  $\alpha$  for  $U_{N10}$  above 10 m s<sup>-1</sup>.

For the drag over continuous ice, L2012 recommend  $C_{DN10i} = 1.6 \times 10^{-3}$ . This is consistent with the range of values for the total drag over large flat floes,  $C_{DN} = 1.2$ -1.9  $\times 10^{-3}$ , given in Overland (1985) making the assumption that the form drag over flat floes is negligible. This choice for  $C_{DN10i}$  is also typical of the values commonly set in numerical models (Lüpkes et al. 2013).

L2012 provides three formulations for the sheltering function,  $S_c$ . The form chosen for the CICE model (Tsamados et al., 2014) is:

$$S_c = \left( 1 - \exp \left( -s \frac{D_w}{h_f} \right) \right), \quad (15)$$

where  $s$  is a dimensionless constant and the distance between floes,  $D_w = \frac{D_i(1-\sqrt{A})}{\sqrt{A}}$  (after Lüpkes and Birnbaum, 2005). Equations (12-15) together with the recommended parameters set out in Table 1 establish the parameterization of  $C_{DN10}$  as a function of  $A$ ,  $h_f$ ,  $D_i$  and  $u_*$ . In many models, however, freeboard heights and floe lengths are not available. In this instance, L2012 provides further simplifications to present both  $h_f$  and  $D_i$  in terms of  $A$ :

$$h_f = h_{max}A + h_{min}(1 - A), \quad (16)$$

$$D_i = D_{min} \left( \frac{A_*}{A_* - A} \right)^\beta, \quad (17)$$

where

$$A_* = \frac{1}{1 - (D_{min}/D_{max})^{1/\beta}} \quad (18)$$

and  $\beta$  is a tuning constant. Recommended values for the constant parameters  $h_{min}$ ,  $h_{max}$ ,  $D_{min}$ ,  $D_{max}$  and  $\beta$  are provided in Table 1, taken from an analysis of laser altimeter observations of these summarised in L2012.

245

### 246 3. Data collection and methodology

#### 247 3.1 Data collection and aircraft instrumentation

248 The data used for this study are from research flights over the Arctic MIZ using two aircraft:  
 249 a DHC6 Twin Otter operated by the British Antarctic Survey and equipped with the Meteorological  
 250 Airborne Science INstrumentation (MASIN) and the UK Facility for Airborne Atmospheric  
 251 Measurement (FAAM) BAe-146. Data from eight flights are used here, conducted between 21 and  
 252 31 March 2013 as part of the first ACCACIA (Aerosol-Cloud Coupling and Climate Interactions in  
 253 the Arctic) field campaign. The relevant flight legs are located both to the northwest of Svalbard  
 254 over Fram Strait and southeast of Svalbard in the Barents Sea (Fig. 1). Wintertime sea ice in the  
 255 Barents Sea is relatively thin and, owing to a cool southward-flowing surface ocean current and  
 256 cyclone activity in the region, tends to extend further South than in Fram Strait where the warm  
 257 North Atlantic Current has a greater influence (Johannessen and Foster, 1978; Sorteberg and  
 258 Kvingedal, 2006).

259 To estimate surface momentum flux from the aircraft requires high frequency measurements  
 260 of wind velocity and altitude; along with an estimate of atmospheric stability. To measure 3D winds  
 261 the MASIN Twin Otter uses a nine-port Best Aircraft Turbulence (BAT) probe (Garman et al.  
 262 2006) mounted on the end of a boom above the cockpit and extending forward of the aircraft's  
 263 nose; while the BAE146 uses a 5-port radome probe on the nose of the aircraft. To measure altitude  
 264 at low levels both aircraft use radar altimeters. To measure air temperatures both aircraft use  
 265 Rosemount sensors (non-deiced and deiced); while to measure sea surface temperature (SST) both  
 266 aircraft use Heimann infrared thermometers. For the calculation of albedo (used to derive estimates  
 267 of sea ice concentration), both aircraft use Eppley PSP pyranometers to measure shortwave  
 268 radiation. Further details about the instrumentation – calibration, sampling rate, resolution and  
 269 accuracy – can be found in King et al. (2008) and Fiedler et al. (2010) for the MASIN Twin Otter;  
 270 and in Renfrew et al. (2008) and Petersen and Renfrew (2009) for turbulence measurements on the  
 271 BAE146. For brevity these details are not reproduced here.

272 In general the aircraft measurements are processed identically. One exception is in the  
 273 calibration of SST. Here the MASIN Twin Otter uses black body calibrations in conjunction with  
 274 corrections for emissivity based on SST measurements of the same surface at different altitudes.  
 275 Whereas for the BAE146 the Heimann infrared SST is adjusted by a constant offset for each flight  
 276 determined by the ARIES (Airborne Research Interferometer Evaluation System) instrument, which  
 277 can estimate the emissivity accurately by rotating the field of view in flight, thus obtaining very  
 278 accurate SST estimates (see Newman et al. 2005; or Cook and Renfrew 2015 for a discussion).

279

### 280 **3.2 Derivation of surface drag coefficients from the aircraft observations**

281 To estimate flight-level momentum flux – from which  $C_{DN10}$  may be derived – we use the  
 282 well-established eddy covariance method. This is commonly used in aircraft-based flux research

(e.g. French et al. 2007) and has previously been used with both MASIN data (e.g. Fiedler et al. 2010; Weiss et al. 2010) and FAAM data (e.g. Petersen and Renfrew 2009; Cook and Renfrew 2015). It requires that flight legs are straight and level and conducted as close to the surface as is logistically feasible (the vast majority of our data were measured at heights under 40 m – see Table 2). These flight legs are then divided into *flux runs* of equal duration, with velocity perturbations calculated from linearly detrended run averages. The flight-level momentum flux ( $\tau$ ) for each run is calculated from the covariance between the perturbation of the horizontal wind components from their means ( $u'$ ,  $v'$ ) and that of the vertical wind component ( $w'$ ) as follows:

$$\tau = \bar{\rho} \sqrt{u'w'^2 + v'w'^2}, \quad (19)$$

where  $\bar{\rho}$  is the mean run air density. It is assumed that the measurements are made in the surface layer, and that this is a constant flux layer so  $\tau$  is not adjusted for height (see Petersen and Renfrew 2009 for a discussion). For the great majority of flights, a mean altitude of ~34 m suggests this is a good assumption. Even so, despite this assumption being widely adopted and generally accepted as necessary, it's accuracy is a point of contention (c.f. Garbrecht et al., 2002) and is an issue for future work. This is more debatable for Flight B760, although discrepancies would be ~5%. The surface roughness length,  $z_0$ , is derived using equations (1) and (2). The stability correction  $\phi$  in Eq. (1) is an empirically derived function of  $z$  and the Obukhov length,  $L$ , a parameter related to stratification. We use the corrections of Dyer (1974) for stable conditions and Beljaars and Holtslag (1991) for unstable conditions. The neutral drag coefficient at 10 m ( $C_{DN10}$ ) is then evaluated for each run via (3).

Each *flux run* is subject to a quality control procedure, details of which can be found in Appendix 1. Through this quality control procedure, it was determined that a *flux-run* length of ~9 km was optimum. For this run length, 14 from the total 209 runs available are rejected following quality control, which leaves a total of 195 usable flux runs.

In order to test our observations against the L2012 parameterization described in section 2 an estimate of the ice fraction  $A$  is required. For this, two methods have been developed using the simultaneous aircraft observations: the first uses albedo (from shortwave radiation); the second uses SST (from the downward infra-red thermometer with some adjustments based on the albedo). The sensitivity to choices made in our estimation of  $A$  in both approaches is tested via the adoption of two different criteria – one based on flight video evidence, the other based on theory. For detailed description of our methodology for estimating  $A$  please see Appendix 2.

## 4. Results

### 4.1 Complete dataset

Our observations enable investigation into the relationship between sea ice drag and ice fraction. Figure 2 shows  $C_{DN10}$  plotted as a function of  $A$  for all *flux-runs* and for all methods used to derive  $A$  (see Appendix 2). These are ice fraction derived via albedo ( $A_a$ ) and via surface temperature ( $A_{SST}$ ) using *no ice transition* tie points set according to inspection of our in-flight videos and also to values expected theoretically ( $A_{SST2}$ ) or as previously observed ( $A_{a2}$ ). The observational data are partitioned into ice fraction bins using intervals in  $A$  of 0.2 (corresponding to a total of 6 bins). This interval was chosen as it permits a relatively large number of data points in each bin (between 11 and 65; see Fig. 2), whilst providing a sufficient number of bins to assess the sensitivity of  $C_{DN10}$  to  $A$ . The distribution of values within each bin is represented by the median, the interquartile range and the 9<sup>th</sup> and 91<sup>st</sup> percentiles.

In all four panels in Fig. 2, the lowest median drag coefficients are found at the upper and lower limits of ice fraction (in the  $A = 0, 0.2$  and 1 bins), whilst the highest median drag coefficients are in the 0.6 and 0.8 bins. This describes a unimodal, negatively skewed distribution (i.e. with a longer tail towards lower  $A$ ). This distribution qualitatively conforms to the L2012 parameterization using typical parameter settings (this is revisited in Section 4.3). Across all ice fractions our results lie within the range of those obtained in previous studies (see review in Section 1 and Andreas et al., 2010).

The small interquartile range in  $C_{DN10}$  evident in Fig. 2 in the  $A = 0$  bin reflects the small variability in wind velocity during the field campaign, with ~~mean (maximum)~~ run-averaged wind speeds ~~averaging of~~  $7 \text{ m s}^{-1}$  (close to the climatological mean for the Arctic summer), peaking at  $13 \text{ m s}^{-1}$  (see Table 2) ~~and being~~ from a generally consistent direction (northerly, i.e. off-ice). Note that over ~~the open ocean-water (away from ice),~~ surface roughness is a strong function of wave height and therefore wind speed. Our bin-averaged  $C_{DN10}$  values over open sea water compare well with those expected by inputting observed wind speeds into the well-established COARE bulk flux algorithm of Fairall et al (2003). Values derived from COARE Version 3.0 consistently lie within the interquartile range.

For data points over continuous ice ( $A = 1$ ) our observed median values of  $C_{DN10}$  are towards the lower end of the range for large flat floes given in Overland (1985) of 1.2-3.7. However, relative to that for  $C_{DN10w}$ , there is a high degree of variability in  $C_{DN10i}$  within bins. This reflects significant heterogeneity in ice conditions and hence roughness, as previously discussed (e.g. Overland, 1985), and as was visually apparent from the aircraft throughout our field campaign. For this reason, over uninterrupted ice  $C_{DN10}$  is region-specific, unlike over open water. In our observations these values are indeed found to vary systematically and considerably with location and this is investigated further below. Even greater scatter in  $C_{DN10}$  is apparent within the



intermediate ice fraction bins (0.2, 0.4, 0.6 and 0.8) as form drag here is affected not only by variability in ice roughness, but also by variability in the frontal area of floes (governed by floe size and freeboard height). Furthermore, the upper limit of ice roughness is likely to be greater here due to deformation as a result of waves and floe advection (Kohout et al., 2014).

It is apparent from Fig. 2 that our results are qualitatively similar for all derivations of  $A$ . In particular, apart for some minor shifts in  $C_{DN10}$  due to the rearrangement of data points between adjacent bins, the impact of varying the *no ice transition* tie point is small (compare panels (a) with (c) and panels (b) with (d)). This implies that our results are relatively robust.

#### 4.2 Variability within the dataset

To further explore the observed sensitivity of  $C_{DN10}$  with  $A$  as well as the scatter in  $C_{DN10}$  within ice fraction bins, we now focus on subsets of the data. Given the dependence of surface roughness not only on ice fraction but also on sea ice properties, a logical divide would be based on location. As apparent in Fig. 1, the flights were conducted either to the northwest of Svalbard in Fram Strait or to the southeast of Svalbard in the Barents Sea. Conveniently, this split apportions approximately equal numbers of data points to each location. Results from Fram Strait are shown in Fig. 3, whilst those from the Barents Sea are shown in Fig. 4. Given the lack of sensitivity of results to varying the *no ice transition* tie point, only  $A_a$  and  $A_{SST}$  are shown here.

Significant differences in the distribution of  $C_{DN10}$  as a function of  $A$  for these two locations are apparent, especially towards the higher ice fractions. The Barents Sea is characterised by far greater values of  $C_{DN10}$  for  $A \geq 0.6$ , with median  $C_{DN10} \approx 2.5 \times 10^{-3}$  at  $A = 1$ , comparing to less than  $1.2 \times 10^{-3}$  in Fram Strait (note that at lower ice fraction there is more consistency in  $C_{DN10}$  between the locations). These differences imply rougher sea ice conditions in the Barents Sea. A result that might be expected given the typically thinner ice, a less sharp ocean-ice transition here (i.e. a geographically larger MIZ, see Fig. 1) and greater variability in the position of the ice edge in the Barents Sea during the field campaign – suggestive of ice melt, deformation and changeable ice conditions. Such heterogeneity is reflected by the considerably greater scatter in  $C_{DN10}$ , whilst the wider MIZ is implied by a considerably larger proportion of data points residing within the intermediate ice fraction bins (0.2, 0.4, 0.6 and 0.8) for the Barents Sea data (around 69%) compared to Fram Strait data (35-51%).

The systematic differences in ice conditions between these locations are also apparent in flight videos and photographs. Figure 5 shows images from two Barents Sea flights: a photograph from the port-side of the FAAM aircraft during Flight B760 and a still taken from the forward-looking video camera ten days later during MASIN Flight 185 (see Fig. 1 for image locations). Each of these images is representative of sea-ice conditions associated with the highest individual

values of  $C_{DN10}$  observed during each flight ( $4.7$  and  $5.7 \times 10^{-3}$  respectively) and correspond to ice fractions of  $\sim 0.8$  and  $\sim 0.6$  respectively. The ice morphology depicted in the two photos is comparable, constituting relatively small, broken floes (order tens of metres in scale) with raised edges implying collisions between the floes. Whilst evidently widespread in the Barents Sea MIZ, such conditions are not apparent in video footage and photographs made during two of the three Fram Strait flights (182 and 183). During these flights, ice morphology in the MIZ appears quite different: consisting of larger floes often separated by large leads and a more distinct ice edge (as depicted for Flight 182 in Fig. 6). The jagged, small floes illustrated in Fig. 5 are associated with high  $C_{DN10}$  values. Such conditions in the wintertime MIZ resemble dynamically rough summertime melt-season ice (Andreas et al., 2010), and smaller floes are associated with greater drag due to an increased frontal area. Note that this roughness extends to the highest ice concentrations (in the  $A = 1$  bin; Fig. 3), despite the fact that floe sizes will tend to increase as  $A$  approaches 1. This is perhaps unsurprising: the photographs of Fig. 5 show that where floes have been fused together – giving a local ice fraction of 1 – the ice noticeably retains its rough, deformed characteristics. Video footage from the third Fram Strait flight (Flight 184) reveals ice conditions more like those observed in the Barents Sea, and indeed this flight was associated with greater drag coefficients than the other two – comparable to those of the Barents Sea flights. Note that whilst the relevant Flight 182 and 183 legs overlap, Flight 184 was conducted further east (Fig. 1).

To delve more deeply into the relationship between  $C_{DN10}$  and ice fraction, we now examine two particular flights – one from each research aircraft. We focus on the flights with the greatest number of *flux-runs* from each aircraft: FAAM Flight B760 and MASIN Flight 181 (Table 2). Figures 7 and 8 show distributions of  $A_a$ ,  $A_{SST}$  and  $C_{DN10}$  for all *flux-runs* in map form for both flights. Note there is generally good agreement between  $A_a$  and  $A_{SST}$  where data is available for both (a pyranometer malfunction during B760 limits the availability of  $A_a$ ). In Flight 181, the aircraft traversed the relatively broken ice immediately south east of Svalbard, and over the ice edge and open water further south. The B760 leg traversed north-south over the ice edge at a similar location. From these figures it is apparent that in general the highest values of  $C_{DN10}$  relate to MIZ conditions. This is especially clear for Flight B760, due to the simple gradient in ice fraction; towards the south,  $C_{DN10}$  is small over open water; moving northward over the MIZ  $C_{DN10}$  increases and exhibits more variability, reflecting typically heterogeneous ice conditions in the MIZ and for the northernmost runs  $C_{DN10}$  decreases again as more consolidated pack ice is encountered (Fig. 7). As discussed above, sea ice conditions during the B760 *flux-run* for which peak  $C_{DN10}$  is observed (arrow in Fig. 7) are captured in the photograph shown in Fig. 5(a).

Figure 9 shows  $C_{DN10}$  as a function of  $A$  for Flight 181. The distribution is similar to that described previously, with  $C_{DN10}$  peaking in the  $A = 0.6$  and  $0.8$  bins. Comparing Fig. 9 with Fig. 3

shows that drag coefficients are towards the lower end of the range for the Barents Sea. Note that a similar plot is not shown for Flight B760 due to the sparsity of data. Of all our flights only 181 provides sufficient data across the range of ice fractions to make presentation in this form worthwhile.

### 4.3 Validation and modifications to the L2012 parameterization

The curves shown in Figures 2, 3, 4 and 9 represent the L2012 parameterization. They result from setting the observed median  $z_{0w}$ ,  $C_{DN10w}$  and  $C_{DN10i}$  in Eq. (12) – to fix the end points of the curves – then adopting new parameter settings for the form component of drag,  $C_{DN10f}$ . These were chosen to provide a good fit to our observational results whilst also largely satisfying previously gathered empirical evidence. In fact, the parameter settings recommended by L2012 provide a near-satisfactory fit to our observations, and only minor optimization is recommended.

Of the parameters dictating the form component of the drag coefficient ( $C_{DN10f}$ ; see Eq. 11),  $h_{min}$ ,  $h_{max}$ ,  $D_{min}$ ,  $D_{max}$  and  $\beta$  are all appointed in L2012 according to previous observations. Values assigned to the effective resistance coefficient  $c_e$  and sheltering parameter  $s$  are considerably less well verified, making them preferential for tuning in the first instance. Increasing  $s$  from the value recommended in L2012 such as to bring about a better fit to our data has minimal effect on  $C_{DN10}$  for all but the highest ice fractions, whereas, as evident from Eq. (12),  $C_{DN10}$  is equally sensitive across the full range of  $A$  to changes in  $c_e$ . Reducing  $c_e$  from 0.3 to 0.17 and keeping all other parameters as recommended in L2012 (E45E2016A in Table 1) provides a generally good fit to our observations and this is illustrated by the black curved lines in Figures 2, 3, 4 and 9. This curve passes close to median values and comfortably through the interquartile range of all ice fraction bins in Fig. 2, demonstrating the skill of the L2012 parameterization in capturing the sensitivity of  $C_{DN10}$  to  $A$  when averaged over a large dataset.

The fit using the E45E2016A settings is not perfect. In particular, there is a suggestion that for the full dataset (Fig. 2)  $C_{DN10}$  is underestimated at high ice fraction (the  $A = 0.8$  and  $0.6$  bins) and overestimated at  $A = 0.2$ . As indicated by our results and those of previous studies,  $C_{DN10}$  at high ice fractions is governed by sea ice morphology and as such its variability is large and location dependent. Consequently, discrepancies here are unsurprising. A possible explanation for the overestimate at lower ice fractions is that the parameterization does not take into account the attenuating effect of sea ice on waves (e.g. Wadhams et al., 1988). To compute the form drag coefficient (Eq. 11) we use observed  $z_{0w}$ , averaged over all *flux-runs* where  $A = 0$ . In the MIZ, this assumes these values to be representative of the water between ice floes. However, given the

sensitivity of  $z_0$  to wave amplitude (discussed in Section 4.1) and the attenuation of waves in the MIZ, these values may in fact be overestimates, leading to an overestimation of  $C_{DN10}$ .

With these discrepancies in mind, we define a second set of parameters, for which  $\beta$  (a morphological exponent describing the dependence of  $D_i$  on  $A$ ) is adjusted as well as  $c_e$ . In L2012 a  $\beta$  value of 1 is derived empirically by fitting their parameterization for  $D_i$  (Eq. 17) to laser scanner observations from Fram Strait obtained by Hartmann et al. (1992) and Kottmeier et al. (1994). However, L2012 also found that by changing only  $\beta$ , their parameterization was able to explain the variability in  $C_{DN10}$  derived from various observational sources. For example,  $\beta = 1.4$  better represented observations made during REFLEX in the eastern Fram Strait (Hartmann et al., 1994), whilst  $\beta = 0.3$  better represented observations made in the Antarctic (Andreas et al., 1984) and the western Fram Strait (Guest and Davidson, 1987). Reducing  $\beta$  has the effect of reducing  $D_i$  and consequently amplifying  $C_{DN10}$  for all ice fractions, though particularly towards the higher fractions (though note  $D_i$  will always eventually converge on  $D_{max}$  at  $A = 1$ , according to Eq. 17). Consequently, setting a low value for  $\beta$  helps explain particularly high drag coefficients at  $A \approx 0.8$ , justifying our second parameter set, for which we reduce  $\beta$  to 0.2 (the lowest value recommended in L2012) in addition to further reducing  $c_e$  to 0.13, to account for the reduction in  $C_{DN10}$  across all values of  $A$  which comes from reducing  $\beta$ . Figure 2 shows that these parameter settings (E15E2016B in Table 1) provide in general a marginally better fit to the complete dataset than the E15E2016A settings.

The parameterization is shown to also provide a generally good fit to subsets of the data. For example, the black and grey curves in Figures 3 and 4 (the Barents Sea and Fram Strait subsets) denote as before the scheme using the E15E2016A and E15E2016B parameter settings respectively, and fit well despite the different ice morphologies and related contrasting values of  $C_{DN10}$  at  $A = 1$ . For the Barents Sea observations, the curve again passes through the interquartile range of all bins – though a little higher than the median values – both for  $A_a$  and  $A_{SST}$ . For the Fram Strait observations there is good agreement in the case of  $A_a$ , whilst for  $A_{SST}$  the form drag is generally overestimated. Finally, the parameterization also provides an accurate representation of the Flight 181 observations (Fig. 9). It is important to note that the success of the scheme for different localities characterised by different ice conditions depends crucially on an accurate representation of  $C_{DN10}$  at  $A = 1$ . As mentioned in Section 2.3, in Eq. 12,  $C_{DN10}$  at  $A = 1$  is provided by  $C_{DN10i}$ , defined in L2012 as *the skin drag over sea ice*. However, given that over rough, ridged sea ice, there is a form drag component in addition to skin drag, this term is more suitably expanded and expressed as *the total (skin and form) drag over continuous sea ice*, and considered to be a variable quantity, dependent on ice conditions.

As discussed in Section 4.2, our observations suggest that ice conditions in the MIZ characterised by relatively small, unconsolidated ‘pancake’ ice floes at intermediate ice concentrations are characterised by higher drag coefficients than larger floes. The roughness extends locally to the highest ice concentrations, suggesting a case could be made for the use of  $D_i$  at intermediate ice fractions as a proxy for local MIZ surface roughness. Although this is partially implicit in the L2012 scheme in the sense that it accounts for smaller floes exerting greater [form drag](#) for a given ice concentration due to a greater frontal area ([c.f. Equation 11](#)), it seems likely given our observations that smaller floes are often associated with larger  $C_{DN10}$  due to other, unaccounted-for reasons. For example, greater deformation and ridge-forming as a result of more frequent floe collisions due to smaller gaps between the floes or to floe advection caused by reduced ocean wave attenuation in areas of smaller floes. Note that this additional roughness corresponds to that discussed in the above paragraph as requiring inclusion in the  $C_{DN10i}$  term in Eq. 12.

[Accounting for variability in the surface roughness of continuous sea ice has previously received some attention in the literature \(Garbrecht et al., 2002; Andreas, 2011\), though there is as yet no clear solution to this problem, and further](#) However, progress in this area is beyond the scope of this study; see Conclusions for recommendations for future work.

## 5. Implications and parameterization recommendations

It is clear that the physically-based parameterization of L2012 qualitatively fits our observations of surface drag (i.e. momentum exchange) over the MIZ very well. The recommended settings provided by L2012 (see Table 1) also quantitatively fit our observations well, although with some tuning of  $c_e$  (the effective resistance coefficient) and, optionally,  $\beta$  (a sea-ice morphology exponent) this fit can be improved when compared to median  $C_{DN10}$  values – see Figures 2-4 and 9. We recommend two settings for the L2012 parameterization: [E15E2016A](#) with  $c_e = 0.17$  and  $\beta = 1$  and [E15E2016B](#) with  $c_e = 0.1$  and  $\beta = 0.2$  (see Table 1). The [E15E2016B](#) setting enhances the negative skew of the  $C_{DN10}$  distribution, increasing (decreasing) values at high (low) ice concentrations. These settings are illustrated as the black and grey lines in Figures 2-4 and 9.

Our recommended L2012 settings are also plotted in Fig. 10 to allow a comparison against several other parameterizations used in numerical sea-ice, climate or weather prediction models.

Fig. 10(a) shows the effective 10-m neutral drag coefficient for a grid square with the ice concentration indicated, i.e. it is an *effective*  $C_{DN10}$  calculated proportionally for that mix of water and sea ice. To allow a direct comparison the drag coefficient over open water,  $C_{DN10w}$ , is set to  $1.1 \times 10^{-3}$  for all the algorithms. This value is appropriate for low-level winds of about  $5 \text{ m s}^{-1}$ . It is simply chosen for illustrative purposes; similar illustrations result for other values of  $C_{DN10w}$ . [Fig. 10\(b\) shows the effective roughness length – derived from the effective  \$C\_{DN10}\$  using equation \(3\) –](#)

523 [as a function of sea ice concentration](#). In addition to our recommended L2012 parameterization  
 524 settings, we also show those set as default in the sea-ice model CICE version 5.1 (see Tsamados et  
 525 al. 2014; Hunke et al. 2015). In these  $c_e = 0.21$ ,  $\beta = 1$  and the ice flow sheltering constant  $s = 0.18$   
 526 (see Table 1). Note there is a typographical error in Table 2 of Tsamados et al. (2014), where the  
 527 parameters  $c_{sf}$  and  $c_{sp}$  are listed as equal to 0.2 (implying  $c_e = 1$ ) when these should have been listed  
 528 as equal to 1 (M. Tsamados, personal communication, 2015). When the corrected values are used,  
 529 the CICE5.1 parameterization matches our observations reasonably well (Figure 10); although it  
 530 does not account for the negative skew in the observations. The unusually large  $c_e$  explains the  
 531 relatively high  $C_{DN10}$  values over the MIZ. Although not unrealistic, these high values are not  
 532 supported by our observations of  $C_{DN10}$ : they are outside the interquartile ranges (Fig. 2). They  
 533 were set in Tsamados et al. (2014) to enable a consistency between the sea-ice form drag on the  
 534 atmosphere and on the ocean, and to help ‘tune’ the CICE simulations of sea ice extent.

535 The ECMWF introduced a new parameterization of surface drag over sea ice in cycle 41 of  
 536 the Integrated Forecast System, which became operational on 12 May 2015. This introduces a  
 537 variable sea-ice roughness length  $z_{0i} = \max [1, 0.93(1 - A) + 6.05e^{-17(A-0.5)^2}] \cdot 10^{-3}$  (see  
 538 ECMWF documentation and Bidlot et al. 2014). This parameterized an increase in drag coefficient  
 539 over the MIZ which was inspired by the observations described in Andreas et al. (2010), so is  
 540 consistent with L2012, and is close to our recommended settings for L2012 (Fig. 10).

541 All of the other parameterizations that are illustrated linearly interpolate between the drag  
 542 coefficient over open water and constant values for  $C_{DN10i}$  (or  $z_{0i}$ ). Consequently they appear as  
 543 straight lines on Fig. 10. In the case of the ECMWF (cycle 40 and earlier) a constant  $z_{0i} = 1 \times 10^{-3}$  m  
 544 (equivalent to  $C_{DN10i} = 1.89 \times 10^{-3}$ ) is set. This is also the default setting in the ECHAM climate  
 545 model (see Lüpkes et al., 2013) and in the WRF numerical weather prediction model (Hines et al.,  
 546 2015) – not shown in Fig. 10. In the CCSM (Community Climate System Model) and CAM5  
 547 (Community Atmospheric Model)  $C_{DN10i}$  is set to  $1.6 \times 10^{-3}$  (see Neale et al. 2010) and in LIM3 (the  
 548 Louvain-la-Neuve Sea Ice Model)  $C_{DN10i}$  is set to  $1.5 \times 10^{-3}$  by default (see Vancoppenolle et al.,  
 549 2012). Previous versions of the CICE sea-ice model also used a constant  $z_{0i}$  set as  $0.5 \times 10^{-3}$  m. The  
 550 Met Office use separate constant values for ‘the MIZ’ (set at  $A = 0.7$ ) and ‘full sea ice’ and then  
 551 linearly interpolate. For their HadGEM3 climate model both  $z_{0i}$  and  $z_{0MIZ}$  are set to  $0.5 \times 10^{-3}$  m for  
 552 version 4.0 of their Global Sea Ice (GSI) configuration, as illustrated in Fig 10; while for UKESM1,  
 553 using GSI6.0, much higher values of  $z_{0i} = 3 \times 10^{-3}$  m and  $z_{0MIZ} = 100 \times 10^{-3}$  m are planned (see Rae  
 554 et al. 2015). These are equivalent to  $C_{DN10}$  values of 2.4 and  $7.5 \times 10^{-3}$ , respectively, so are *not*  
 555 supported by our observations (see Fig. 2).

Formatted: Font: Italic

Formatted: Font: Italic

Formatted: Font: Italic

Examining Fig. 10, only the new (cycle 41) ECMWF parameterization is qualitatively and quantitatively comparable to our recommended settings of the L2012 parameterization. At present most numerical weather and climate prediction models do not have a maximum in drag coefficient over the MIZ. Consequently they are not consistent with our observations, nor those of relevant previous compilations (e.g. Andreas et al., 2010; L2012).

It is clear that in configuring sea ice models,  $C_{DN10}$  over sea ice has commonly been used as a ‘tuning parameter’. In fact it was specifically treated as such in the model sensitivity studies of, for example, Miller et al. (2006) and Rae et al. (2014). Miller et al. (2006) used the CICE model in standalone mode and varied three parameters widely, including  $C_{DN10}$  between  $0.3\text{--}1.6 \times 10^{-3}$ , in an optimisation exercise. They found significant variability in extent and thickness across their simulations and concluded that determining an optimal set of parameters depended heavily on the forcing and validation data used. Rae et al. (2014) carried out a comprehensive fully coupled atmosphere-ocean-ice modelling sensitivity study, testing a large number of sea-ice related parameter settings within their observational bounds. They found statistically significant sensitivity to the two sets of roughness length settings they tested: ‘CTRL’ ( $z_{0i} = 0.5 \times 10^{-3}$  and  $z_{0MIZ} = 0.5 \times 10^{-3}$  m) and ‘ROUGH’ ( $z_{0i} = 3 \times 10^{-3}$  and  $z_{0MIZ} = 100 \times 10^{-3}$  m). The rougher settings (also consistent with those in the Met Office global operational model) generally lead to simulations with a better sea-ice extent and volume compared to observations. However we would note again, that they are not consistent with our observations. Instead our results would suggest these seemingly required large roughness lengths must be compensating for other deficiencies in the model configuration.

As discussed in Section 2, the exchange of momentum between the atmosphere and sea ice depends heavily on sea-ice morphology, thickness and concentration. Prior to this study, observations of sea-ice drag were relatively limited, especially for the MIZ (i.e. for ice fractions  $0 < A < 1$ ). Consequently  $C_{DN10}$  has not previously been well constrained by observations. Our data set doubles the number of observations available over the MIZ and is based on independent research platforms and analysis procedures to previously published data sets. Importantly our results are broadly consistent with these previous observational compilations (e.g. Andreas et al. 2010; and L2012). This corroboration provides further confidence in our recommendations. In short,  $C_{DN10}$  is now better constrained and we recommend its parameterization is consistent with our results.

## 6. Conclusions

We have investigated surface momentum exchange over the Arctic marginal ice zone using what is currently the largest set of aircraft observed data of its kind. Our results show that the momentum exchange is sensitive to sea ice concentration and morphology. Neutral 10-m surface

drag coefficients ( $C_{DN10}$ ) are derived using the eddy covariance method and Monin-Obukhov theory, and two methods (which provide qualitatively similar results) are adopted for the derivation of ice fraction from our aircraft observations. After averaging  $C_{DN10}$  data into ice fraction bins, the roughest surface conditions (characterised by the highest surface drag coefficients) are typically found in the ice fraction bins of 0.6 and 0.8; whilst the smoothest surface conditions tend to be over open water and sometimes (dependent on sea ice conditions) over continuous sea ice. Consequently, a good approximation for our observed  $C_{DN10}$  as a function of ice concentration is provided by a negatively skewed distribution, in general agreement with previous observational studies (Hartman et al., 1994; Mai et al., 1996; Lüpkes and Birnbaum, 2005). However, we have found systematic differences in roughness between different locations. Over deformed, 10-m scale pancake ice in the Barents Sea, drag coefficients are considerably greater than over relatively homogenous, non-deformed sea ice in Fram Strait. This dependence on ice morphology governs the magnitude and variability with ice fraction of  $C_{DN10}$ , and is likely to be the major cause of the considerable scatter in  $C_{DN10}$  within each ice fraction bin.

Our observations have been used as a means to validate and tune one of the leading sea ice drag parameterization schemes – that of Lüpkes et al. (2012) i.e. L2012. This scheme provides  $C_{DN10}$  as the sum of the drag over open water and continuous sea ice, and the form drag on ice floe edges, as given in Eq. 12 and repeated here:

$$C_{DN10} = (1 - A)C_{DN10w} + AC_{DN10i} + A \frac{h_f}{D_i} S_c^2 \frac{c_e}{2} \left[ \frac{\ln^2(h_f/z_{0w})}{\ln^2(10/z_{0w})} \right].$$

The final term on the right hand side of this equation expresses the form drag component, and is derived following the theory of pressure drag exerted on a bluff body. This expression can be simplified following L2012 to be given as a function of only ice fraction  $A$  and tuneable constants via equations 15 to 18. In this simple form, the scheme provides a generally accurate representation of the observed distribution of  $C_{DN10}$  as a function of sea ice fraction. The agreement is optimized by adopting minor parameter adjustments to those originally recommended in L2012. These new settings are labelled as [E45E2016A](#) and [E45E2016B](#) in Table 1. [E45E2016B](#) arguably provides a better fit, though with values of  $c_e$  and  $\beta$  which are at the limit of those physically plausible according to observations, whereas for [E45E2016A](#) these values are well within the confines of those observed. The scheme is shown to be robust; its success holding for subsets of our data (e.g. for each of the Barents Sea and Fram Strait locations, and for the single flight with the greatest number of data points) so long as it is anchored at  $A = 1$  by an observed value for  $C_{DN10i}$ .

Given the success of a sophisticated scheme such as that of L2012, the representation of sea ice drag in many weather and climate models seems crude by comparison, with  $C_{DN10}$  often set with little consideration of physical constraints and instead used as a tuning parameter. Our



comprehensive observations provide the best means yet to constrain parameterizations of  $C_{DN10}$  over the MIZ. They clearly imply that linearly interpolating between the open water surface drag ( $C_{DN10w}$ ) and a fixed sea-ice surface drag ( $C_{DN10i}$ ), as many parameterizations do, is not physically justified or representative. It is recommended that, as a minimum, parameterizations incorporate a peak in  $C_{DN10}$  within the range  $A = 0.6$  to  $0.8$  (as a guide, in the  $0.6$  and  $0.8$  ice fraction bins of our observations,  $C_{DN10}$  has a mean interquartile range of  $1.25$  to  $2.85 \times 10^{-3}$  for all data – i.e. averaged across both bins for all panels in Fig. 2). [Note that the precise peak value will vary with sea ice morphology and, as found in Lüpkes and Gryanik \(2015\), stratification.](#) Though sophisticated, the simplest form of the L2012 scheme is not computationally complex (having only one independent variable,  $A$ ) and is recommended for adoption in weather and climate models.

The sensitivity of  $C_{DN10}$  to ice fraction is now well established. Consequently we recommend that future work focuses on the remaining major source of uncertainty: sensitivity to ice morphology. Our results suggest that the simplification of the L2012 scheme by parameterizing floe dimension ( $D_i$ ) and freeboard ( $h_f$ ) in its expression for form drag [on floe edges](#) using  $A$  provides sufficiently accurate results. Even so, as discussed above, floe size and ice morphology has a major impact on surface roughness and a more sophisticated representation of this should benefit sea-ice and climate simulations. In particular, this study demonstrates that setting an appropriate value of  $C_{DN10}$  at  $A = 1$  is vital to the success of the L2012 parameterization; given the observed variation with location (and hence ice conditions), a constant value for  $C_{DN10}$  at  $A = 1$  is clearly unsuitable for simulations over large areas such as the entire Arctic. Here, we simply vary  $C_{DN10i}$  in the L2012 scheme to reflect the observed location-dependent ice roughness at  $A = 1$ . In sea-ice or climate models, perhaps  $C_{DN10}$  at  $A = 1$  should be determined from sea-ice model output – for example, Tsamados et al. (2014) account for form drag on ice ridges. In operational models, perhaps  $C_{DN10}$  at  $A = 1$  should be derived from sea-ice thickness observations (e.g. from CryoSat-2).

Our observations indicate that floe size is a governing factor in local variations of sea ice roughness, even at the highest ice fractions. Consequently, to account for MIZ roughness associated with local ice conditions an option could be to accentuate the dependency of  $C_{DN10}$  on floe size by expanding  $C_{DN10i}$  to incorporate both the skin drag term and an additional ‘local’ sea ice form drag term which would be inversely proportional to a representative value of  $D_i$  (e.g. average  $D_i$  at a given ice fraction). To pursue such an approach and in general to provide clarity on this issue, future work would benefit greatly from incorporating aircraft laser scanner data, from which detailed morphological information on sea ice conditions including floe shape, size, thickness and roughness features such as ridging can be derived.

## Acknowledgements

This work was funded by NERC (grants numbers NE/I028653/1, NE/I028858/1 and NE/I028297/1) as part of its Arctic Research Programme. We thank the FAAM and MASIN pilots, crew, flight planners and mission scientists; Christof Lüpkes, Jean Bidlot, Jamie Rae and John Edwards for discussions; and Barbara Brooks for providing photographs.

## Appendix 1: Quality control of momentum flux data

In order to remove unsuitable data, a quality control procedure is utilised. This procedure follows previous studies (e.g. French et al., 2007; Petersen and Renfrew, 2009; Cook and Renfrew, 2015) and involves the visual inspection of a series of statistical diagnostics describing the variability of the perturbation wind components along each *flux-run*. ‘Bad’ data points arise as a result of instrument malfunction or the violation of assumptions made in the methodology – notably that the turbulence is homogenous along each run. The criteria that determine a ‘good’ run are as follows:

- The power spectra of the along-wind velocity component should have a well-defined decay slope (close to  $k^{-5/3}$  for wavenumber  $k$ ).
- The total covariance of the along-wind velocity and vertical velocity should be far greater in magnitude than that of the cross-wind velocity and vertical velocity (which should be small) indicating alignment of the shear and stress vectors.
- The cumulative summation of the covariance of the along-wind velocity and the vertical velocity should be close to a constant slope, indicating homogeneous covariance.
- The cospectra of the covariance of the along-wind velocity and the vertical velocity should have little power at wavenumbers smaller than about  $10^{-4} \text{ m}^{-1}$ , implying that mesoscale circulation features are not contributing significantly to the stress.
- The cumulative summation of the cospectra should be shaped as ogives (‘S’-shaped, with flat ends) implying that all of the wavenumbers that contribute to the total stress have been sampled and again that mesoscale features are not present.

Examples of ‘good’ and discarded runs are illustrated in Fig. A1 (where the *flux-run* length is ~9 km). In the ‘good’ example, there is little cross-wind spectral power and the cumulative summation has a near constant slope indicating homogenous turbulence structure along the length of the run. The ‘S’-shaped ogives and lack of power at small wavenumbers in the co-spectra suggest that the turbulence is fully captured and that the signal is ‘unpolluted’ by mesoscale circulations. For this typical case, the majority of energy is in eddies ranging from about 30 to 500 m in size, with no energy at all for wavelengths over 2500 m. This information helps inform a suitable run duration, since it is important that the runs are long enough to capture several eddies of sizes at least

across the dominant range of the spectrum. On the other hand, lengthening runs reduces the number of data points and increases the risk of sampling organised mesoscale features instead of pure turbulence.

Note five different *flux-run* durations were trialled using a sample of the dataset. These durations varied between the two aircraft (according to their mean flight speed) in order that they correspond to lengths of approximately 3, 6, 9, 12 and 15 km. Using the above quality control procedure it was ascertained that a run length of 9 km procures the highest quality data and so is used here. This is comparable to Weiss et al. (2010) and Fiedler et al. (2010) who used 8 and 8.8 km; and a little shorter than Petersen and Renfrew (2009) and Cook and Renfrew (2015) who used 12 km.

## Appendix 2 – Deriving ice fraction $A$ from the aircraft observations

Two different remote sensing techniques are used to derive estimates of *ice fraction*  $A$  from the aircraft observations, using proxies based on albedo and surface temperature. These techniques rely on sea ice being more reflective and colder than sea water. In both approaches the proxy is linked to  $A$  using two tie points: one at the *no ice transition* between open water and the onset of ice ( $A \rightarrow 0$ ) and another at the *all ice transition* between continuous ice and the appearance of some water ( $A \rightarrow 1$ ). This allows an estimate of ice concentration for each data point, accounting for the fact that each measurement may sample multiple floes. Ice fraction is then provided for each measurement by

$$A_X = \begin{cases} 0 & \text{for } X \leq X_{A \rightarrow 0} \\ \frac{(X - X_{A \rightarrow 0})}{(X_{A \rightarrow 1} - X_{A \rightarrow 0})} & \text{for } X_{A \rightarrow 0} < X < X_{A \rightarrow 1} \\ 1 & \text{for } X \geq X_{A \rightarrow 1} \end{cases}, \quad (20)$$

where  $X$  is the instantaneous value of the proxy and  $X_{A \rightarrow 0}$  and  $X_{A \rightarrow 1}$  are the tie points for the *no ice transition* and the *all ice transition* respectively. Note that the recorded aircraft data (1 Hz for the relevant diagnostics) and approximate mean aircraft speed for straight and level runs (60 and 100 m s<sup>-1</sup> for MASIN and FAAM respectively) translates to each measurement point sampling over a distance of 60 and 100 m ( $\gg D_{min}$ ) respectively. We average over the 9-km run to obtain a representative ice fraction  $A$ .

Albedo is calculated from measurements of the upward and downward components of the shortwave radiative flux:  $a = SW_U/SW_D$ .  $A_a$  is derived using tie points  $a_{A \rightarrow 0} = 0.15$  and  $a_{A \rightarrow 1} = 0.85$ , which were chosen following careful review of video footage from four flights (two from each aircraft: MASIN 182 and 185; FAAM B761 and B765). It is accepted that these tie points are approximate and may vary depending on ice conditions, however there is good agreement between the flights for which video footage was available. Whilst these values are broadly consistent with

727 textbook albedo values (e.g. Curry and Webster 1999),  $a_{A \rightarrow 0}$  is towards the upper end of the  
 728 expected range, so an alternative albedo-derived ice fraction,  $A_{a2}$ , is calculated using  $a_{A \rightarrow 0} = 0.07$   
 729 (matching that used to approximate freezing point in the Weddell Sea in Weiss et al., 2012). A  
 730 limitation of the albedo approach is that  $A_a$  will be underestimated for semi-transparent thin ice, as  
 731 measurements will be affected by the lower albedo of the sea water below.

732 In the sea surface temperature (*SST*) approach, a lower tie point of  $SST_{A \rightarrow 0} = -3.4$  °C was  
 733 ascertained following inspection of the flight videos. It is recognised that this value is lower than  
 734 might be expected given typical ocean salinity. Indeed, salinity measurements made by the *RRS*  
 735 *James Clark Ross* as part of the ACCACIA field campaign suggests typical values of between 30  
 736 and 35 (a little fresher than is typical, likely as a result of spring melt), implying a freezing point of  
 737 about -1.8 °C. It is possible this discrepancy may be due to a cool skin being measured by the  
 738 aircraft's radiometers. In the vicinity of the MIZ, cool skin temperatures are likely to be a result of  
 739 the top few centimetres of the ocean containing small fragments of ice (e.g. frazil) as was observed  
 740 during the flights. In addition the radiatively driven 'cool skin effect' (Fairall et al., 1996) may also  
 741 contribute. To account for this uncertainty, we also calculate two different ice fractions using the  
 742 *SST* approach;  $A_{SST}$  uses the lower value suggested by the video footage (-3.4 °C), whilst  $A_{SST2}$   
 743 uses the theoretical value based on observed salinities (-1.8 °C).

744 Due to the thin-ice problem, the *SST* approach is arguably more suitable than the albedo  
 745 approach at prescribing the onset of ice with a suitable fixed *no ice transition* (so long as a suitable  
 746 value is determined). However, there is a fundamental problem in assigning an *SST all ice*  
 747 *transition* that is suitable across multiple flights. This is because the surface temperature over  
 748 continuous ice varies greatly according to the atmospheric conditions. Using a fixed value for  
 749  $SST_{A \rightarrow 1}$  could therefore lead to inconsistencies between flights under different weather conditions;  
 750 for example overestimating  $A$  in the case of particularly cold ice floes as  $A \rightarrow 1$ . Consequently in  
 751 the *SST* approach an adjustment of the  $SST_{A \rightarrow 1}$  tie point using albedo is used, which provides a  
 752 robust estimate of  $SST_{A \rightarrow 1}$  for any atmospheric conditions. For each flight,  $SST_{A \rightarrow 1}$  is set equal to  
 753 the median *SST* value for all *flux-run* data points where  $a$  is within the range  $a_{A \rightarrow 1} \pm 0.05$ , i.e.  
 754 between 0.8 and 0.9. Using this criterion,  $SST_{A \rightarrow 1}$  ranges from -23.6 to -9.6 °C between flights, with  
 755 this variability being a strong function of latitude (the colder values being for the northernmost  
 756 flights). The suitability of this method is demonstrated by the high level of internal consistency in  
 757 *SST* values within the  $a_{A \rightarrow 1} \pm 0.05$  range for each flight, with a mean standard deviation (averaged  
 758 across all flights) of only 1.3 °C.

759 Figure A2 compares the ice fractions estimated using the albedo and *SST* methods. It shows  
 760 there is a near one-to-one relationship between  $A_a$  and  $A_{SST}$ , with a correlation coefficient of 0.94, a

761 root-mean-square error of 0.12 and a bias error of 0.03 for the video-assigned values of  $a_{A \rightarrow 0}$  and  
762  $SST_{A \rightarrow 0}$ . Linear regressions with the alternative tie point values show only a small sensitivity to  
763 these settings. Overall Fig. A2 demonstrates our methodologies are sound and the estimates of ice  
764 fraction are robust.

765 **Notation**

766	$A$	ice fraction
767	$\alpha$	Charnock constant
768	$b$	smooth flow constant for the Charnock relation
769	$\beta$	constant exponent describing the dependence of $D_i$ on $A$
770	$C_D$	drag coefficient
771	$C_{DN10}$	drag coefficient for neutral stability at a height of 10 metres
772	$C_{DNf10}$	neutral form drag coefficient at a height of 10 metres
773	$C_{DNI10}$	neutral drag coefficient over sea ice at a height of 10 metres
774	$C_{DNw10}$	neutral drag coefficient over sea water at a height of 10 metres
775	$c_e$	effective resistance coefficient
776	$c_s$	ice floe shape parameter
777	$c_w$	fraction of the available force acting on each floe
778	$D_i$	cross-wind floe dimension
779	$D_{min}, D_{max}$	minimum and maximum cross-wind floe dimension
780	$D_w$	distance between floes
781	$f_d$	total force acting on the frontal areas of ice floes within the area $S_t$
782	$h_f$	freeboard height of floes
783	$h_{min}, h_{max}$	minimum and maximum freeboard height of floes
784	$\kappa$	von Karman constant (0.4)
785	$N$	number of floes in area $S_t$
786	$\rho$	air density
787	$s$	ice floe sheltering function constant
788	$S_c$	ice floe sheltering function
789	$S_t$	domain area of $N$ floes
790	$\tau$	momentum flux
791	$\tau_d$	momentum flux related to form drag
792	$U$	horizontal wind speed
793	$U_{10N}$	adjusted 10-m neutral horizontal wind speed
794	$u_*$	friction velocity
795	$\nu$	dynamic viscosity
796	$\varphi$	Monin-Obukhov stability correction
797	$z_0$	roughness length
798	$z_{0i}$	roughness length for sea ice
799	$z_{0w}$	roughness length for open water

800

## References

[Andreas, E. L.: A relationship between the aerodynamic and physical roughness of winter sea ice. Q. J. R. Meteorol. Soc., 137, 927-943, 2011.](#)

Andreas, E. L., Horst, T. W., Grachev, A. A., Persson, P. O. G., Fairall, C. W., Guest, P. S., and Jordan, R. E.: Parametrizing turbulent exchange over summer sea ice and the marginal ice zone. Q. J. Roy. Meteor. Soc., 136(649), 927-943, doi:10.1002/qj.618, 2010.

Andreas, E. L., Tucker, W. B., and Ackley, S. F.: Atmospheric boundary-layer modification, drag coefficient, and surface heat flux in the Antarctic marginal ice zone. J. Geophys. Res. Oceans (1978–2012), 89(C1), 649-661, doi:10.1029/JC089iC01p00649, 1984.

Arya, S. P. S.: Contribution of form drag on pressure ridges to the air stress on Arctic ice. J. Geophys. Res., 78(30), 7092-7099, doi:10.1029/JC078i030p07092, 1973.

Arya, S. P. S.: A drag partition theory for determining the large-scale roughness parameter and wind stress on the Arctic pack ice. J. Geophys. Res., 80(24), 3447-3454, doi: 10.1029/JC080i024p03447, 1975.

Banke, E. G., and Smith, S. D.: Wind stress over ice and over water in the Beaufort Sea. J. Geophys. Res., 76(30), 7368-7374, doi:10.1029/JC076i030p07368, 1971.

Beljaars, A. C. M., and Holtslag, A. A. M.: Flux parameterization over land surfaces for atmospheric models. J Appl Meteorol, 30(3), 327-341, 10.1175/1520-0450(1991)030<0327:FPOLSF>2.0.CO;2, 1991.

Bidlot, J.-R., Keeley S., and Mogensen, K.: Towards the Inclusion of Sea Ice Attenuation in an Operational Wave Model. Proceedings of the 22nd IAHR International Symposium on ICE 2014 (IAHR-ICE 2014), available at <http://rpsonline.com.sg/iahr-ice14/html/org.html>, 2014.

Birnbaum, G., and Lüpkes C.: A new parameterization of surface drag in the marginal sea ice zone. Tellus 54A, 107–123., doi:10.1034/j.1600-0870.2002.00243.x, 2002.

Brown, E. N., Friehe, C. A., and Lenschow, D. H.: The use of pressure fluctuations on the nose of an aircraft for measuring air motion. J. Clim. Appl. Meteorol., 22(1), 171-180, 10.1175/1520-0450(1983)022<0171:TUOPFO>2.0.CO;2, 1983.

Businger, J. A.: Equations and concepts. Pp. 1–36 in Atmospheric Turbulence and Air Pollution Modeling. Reidel: Dordrecht, 10.1007/978-94-010-9112-1\_1, 1982.

[Castellani, G., Lüpkes, C., Hendricks, S., and Gerdes, R.: Variability of Arctic sea-ice topography and its impact on the atmospheric surface drag, J. Geophys. Res. Oceans, 119\(10\), 6743-6762, doi:10.1002/2013JC009712, 2014.](#)

Claussen, M.: Area-averaging of surface fluxes in a neutrally stratified, horizontally inhomogeneous atmospheric boundary layer, Atmos Environ, 24A, 1349–1360, 1990.

- 835 Cook, P. A., and Renfrew, I. A.: Aircraft-based observations of air–sea turbulent fluxes around the  
836 British Isles. *Q. J. Roy. Meteor. Soc.*, 141(686), 139–152, 10.1002/qj.2345, 2015.
- 837 Dyer, A. J.: A review of flux-profile relationships. *Bound.-Lay. Meteorol.*, 7(3), 363–372,  
838 10.1007/BF00240838, 1974.
- 839 ECMWF: Working Group Report: ECMWF-WWRP/THORPEX Polar Prediction Workshop  
840 ([http://www.ecmwf.int/newsevents/meetings/workshops/2013/Polar\\_prediction/](http://www.ecmwf.int/newsevents/meetings/workshops/2013/Polar_prediction/)), 2013
- 841 Fairall, C. W., Bradley, E. F., Godfrey, J. S., Wick, G. A., Edson, J. B., and Young, G. S.:  
842 Cool-skin and warm-layer effects on sea surface temperature. *J. Geophys. Res. Oceans*  
843 (1978–2012), 101(C1), 1295–1308, 10.1029/95JC03190, 1996.
- 844 Fairall, C. W., Bradley, E. F., Hare, J. E., Grachev, A. A., and Edson, J. B.: Bulk parameterization  
845 of air-sea fluxes: Updates and verification for the COARE algorithm. *J. Climate*, 16, 571–  
846 591, doi:10.1175/1520-0442(2003)016<0571:BPOASF>2.0.CO;2, 2003.
- 847 Fiedler, E. K., Lachlan-Cope, T. A., Renfrew, I. A., and King, J. C.: Convective heat transfer over  
848 thin ice covered coastal polynyas, *J. Geophys. Res.*, 115, C10051,  
849 doi:10.1029/2009JC005797, 2010.
- 850 French, J. R., Drennan, W. M., Zhang, J. A., and Black, P. G.: Turbulent fluxes in the hurricane  
851 boundary layer. Part I: Momentum flux. *J. Atmos. Sci.*, 64(4), 1089–1102,  
852 doi:10.1175/JAS3887.1, 2007.
- 853 Garbrecht, T., Lüpkes, C., Augstein, E., and Wamser, C.: The influence of a sea ice ridge on the  
854 low level air flow, *J. Geophys. Res.* 104(D20), 24499–24507, doi:10.1029/1999JD900488,  
855 1999.
- 856 Garbrecht, T., Lüpkes, C., Hartmann, J., and Wolff, M.: Atmospheric drag coefficients over sea ice  
857 – validation of a parameterisation concept, *Tellus A*, 54(2), 205–219, doi:10.1034/j.1600-  
858 0870.2002.01253.x, 2002.
- 859 Garman, K. E., Hill, K. A., Wyss, P., Carlsen, M., Zimmerman, J. R., Stirm, B. H., Carney, T. Q.,  
860 Santini, R., and Shepson, P. B.: An Airborne and Wind Tunnel Evaluation of a Wind  
861 Turbulence Measurement System for Aircraft-Based Flux Measurements. *J. Atmos. Ocean*  
862 *Tech.*, 23(12), 1696–1708, doi:10.1175/JTECH1940.1, 2006.
- 863 Guest, P. S., and Davidson, K. L.: The effect of observed ice conditions on the drag coefficient in  
864 the summer East Greenland Sea marginal ice zone. *J. Geophys. Res. Oceans* (1978–  
865 2012), 92(C7), 6943–6954, doi:10.1029/JC092iC07p06943, 1987.
- 866 Hanssen-Bauer, I., and Gjessing, Y. T.: Observations and model calculations of aerodynamic drag  
867 on sea ice in the Fram Strait, *Tellus 40A*, 151–161, doi:10.1111/j.1600-  
868 0870.1988.tb00413.x, 1988.



- Hartmann, J., Kottmeier, C., Wamser, C., and Augstein, E.: Aircraft measured atmospheric momentum, heat and radiation fluxes over Arctic sea ice. *The polar oceans and their role in shaping the global environment*, 443-454, doi:10.1029/GM085p0443, 1994.
- Hines, K. M., Bromwich, D. H., Bai, L., Bitz, C. M., Powers, J. G., and Manning, K. W.: Sea Ice Enhancements to Polar WRF. *Mon. Weather Rev.*, 143, 2363-2385, doi:10.1175/MWR-D-14-00344.1, 2015.
- Hunke, E. C., Lipscomb, W. H., Turner, A. K., Jeffery N., and Elliott, S.: CICE: the Los Alamos Sea Ice Model documentation and software user's manual, Version 5.1, 116 pp, Available: <http://oceans11.lanl.gov/trac/CICE>, 2015.
- Johannessen, O. M., and Foster, L. A.: A note on the topographically controlled oceanic polar front in the Barents Sea. *J. Geophys. Res. Oceans* (1978–2012), 83(C9), 4567-4571, doi:10.1029/JC083iC09p04567, 1978.
- King, J. C., Lachlan-Cope, T. A., Ladkin, R. S., Weiss, A.: Airborne measurements in the stable boundary layer over the Larsen Ice Shelf, Antarctica. *Boundary-Layer Meteorol.* 127, 413–428, doi:10.1007/s10546-008-9271-4, 2008.
- Kwok, R., and Rothrock, D. A.: Decline in Arctic sea ice thickness from submarine and ICESat records: 1958 – 2008, *Geophys. Res. Lett.*, 36, L15501, doi:10.1029/2009GL039035, 2009.
- Kohout, A. L., Williams, M. J. M., Dean, S. M., and Meylan, M. H.: Storm-induced sea-ice breakup and the implications for ice extent. *Nature*, 509(7502), 604-607, doi:10.1038/nature13262, 2014.
- Lüpkes, C., and Birnbaum, G.: Surface drag in the Arctic marginal sea-ice zone: A comparison of different parameterisation concepts. *Bound. Lay. Meteorol.*, 117: 179–211, doi:10.1007/s10546-005-1445-8, 2005.
- Lüpkes, C., and Gryanik, V. M.: A stability-dependent parametrization of transfer coefficients for momentum and heat over polar sea ice to be used in climate models. *J. Geophys. Res. Atmos.*, 120(2), 552-581, doi:10.1002/2014JD022418, 2015.
- Lüpkes, C., Gryanik, V. M., Hartmann, J., and Andreas, E. L.: A parametrization, based on sea ice morphology, of the neutral atmospheric drag coefficients for weather prediction and climate models, *J. Geophys. Res.*, 117, D13112, doi:10.1029/2012JD017630, 2012.
- ~~Lüpkes, C., and Gryanik, V. M.: A stability-dependent parametrization of transfer coefficients for momentum and heat over polar sea ice to be used in climate models. *J. Geophys. Res. Atmos.*, 120(2), 552-581, doi:10.1002/2014JD022418, 2015.~~
- Lüpkes, C., Gryanik, V. M., Rösel, A., Birnbaum, G., and Kaleschke, L.: Effect of sea ice morphology during Arctic summer on atmospheric drag coefficients used in climate models, *Geophys. Res. Lett.*, 40, 446–451, doi:10.1002/grl.50081, 2013.

- 904 Mai, S., Wamser, C., and Kottmeier, C.: Geometric and aerodynamic roughness of sea ice. *Bound.*  
 905 *Lay. Meteorol.*, 77(3-4), 233-248, doi:10.1007/BF00123526, 1996.
- 906 Markus, T., J. C. Stroeve, and J. Miller: Recent changes in Arctic sea ice melt onset, freezeup, and  
 907 melt season length, *J. Geophys. Res.*, 114, C12024, doi:10.1029/2009JC005436, 2009.
- 908 Miller, P. A., Laxon, S. W., Feltham, D. L., and Cresswell, D. J.: Optimization of a sea ice model  
 909 using basinwide observations of Arctic sea ice thickness, extent, and velocity. *J. Climate*,  
 910 19, 1089-1108, doi:10.1175/JCLI3648.1, 2006.
- 911 Neale, R. B., Chen, C. C., Gettelman, A., Lauritzen, P. H., Park, S., Williamson, D. L., Rasch, P. J.,  
 912 Vavrus, S. J., Taylor, M. A., Collins, W. D., Zhang, M. and Shian-Jiann, L.: Description of  
 913 the NCAR Community Atmospheric Model (CAM 5.0), NCAR technical note, NCAR/TN-  
 914 486 + STR, 268 pp, 2010.
- 915 Newman, S. M., Smith, J. A., Glew, M. D., Rogers, S. M., Taylor, J.P.: Temperature and salinity  
 916 dependence of sea surface emissivity in the thermal infrared. *Q. J. Roy. Meteor. Soc.*, 131:  
 917 2539–2557, doi:10.1256/qj.04.150, 2005.
- 918 Notz, D.: Challenges in simulating sea ice in Earth System Models, *Wiley Interdiscip. Rev. Clim.*  
 919 *Change*, 3:509–526. doi:10.1002/wcc.189, 2012.
- 920 Overland, J. E.: Atmospheric boundary layer structure and drag coefficients over sea ice. *J.*  
 921 *Geophys. Res. Oceans* (1978–2012), 90(C5), 9029-9049, doi:10.1029/JC090iC05p09029,  
 922 1985.
- 923 Pellerin, P., Ritchie, H., Saucier, F. J., Roy, F., Desjardins, S., Valin, M., and Lee, V.: Impact of a  
 924 two-way coupling between an atmospheric and an ocean-ice model over the Gulf of St.  
 925 Lawrence. *Mon. Weather Rev.*, 132: 1379–1398, doi:10.1175/1520-  
 926 0493(2004)132<1379:IOATCB>2.0.CO;2, 2004.
- 927 Petersen, G. N., and Renfrew, I. A.: Aircraft-based observations of air–sea fluxes over Denmark  
 928 Strait and the Irminger Sea during high wind speed conditions. *Q. J. Roy. Meteor. Soc.*,  
 929 135(645), 2030-2045, doi:10.1002/qj.355, 2009.
- 930 Rae, J. G. L., Hewitt, H. T., Keen, A. B., Ridley, J. K., Edwards, J. M., and Harris, C. M.: A  
 931 sensitivity study of the sea ice simulation in the global coupled climate model, HadGEM3.  
 932 *Ocean Model.*, 74, 60-76, doi:10.1002/qj.355, 2014.
- 933 Rae, J. G. L., Hewitt, H. T., Keen, A. B., Ridley, J. K., West, A. E., Harris, C. M., Hunke, E. C.,  
 934 and Walters, D.N.: Development of Global Sea Ice 6.0 CICE configuration for the Met  
 935 Office Global Coupled Model, *Geosci. Model Dev. Discuss.*, doi:10.5194/gmdd-8-2529-  
 936 2015, 2015.

- Roy, F., Chevallier, M., Smith, G., Dupont, F., Garric, G., Lemieux, J.-F., Lu, Y., and Davidson, F.: Arctic sea ice and freshwater sensitivity to the treatment of the atmosphere-ice-ocean surface layer. *J. Geophys. Res. Oceans*. doi: 10.1002/2014JC010677, 2015
- Schröder, D., Vihma, T., Kerber, A., and Brümmer, B.: On the parameterisation of Turbulent Surface Fluxes Over Heterogeneous Sea Ice Surfaces, *J. Geophys. Res.*, 108(C6), 3195 doi: 10.1029/2002JC001385, 2003.
- Smith, G. C., Roy, F., Brasnett, B.: Evaluation of an operational ice-ocean analysis and forecasting system for the Gulf of St Lawrence. *Q. J. R. Meteorol. Soc.*, 139: 419–433. doi:10.1002/qj.1982, 2013.
- Sorteberg, A., and Kvingedal, B.: Atmospheric forcing on the Barents Sea winter ice extent. *J. Climate*, 19(19), 4772–4784, 2006.
- Stössel, A., Cheon, W.-G., and Vihma, T.: Interactive momentum flux forcing over sea ice in a global ocean GCM, *J. Geophys. Res.*, 113, C05010, doi:10.1029/2007JC004173, 2008.
- Stull, R. B.: An introduction to boundary layer meteorology, *Kluwer Academic Publishers*, Dordrecht, doi:10.1007/978-94-009-3027-8, 1988.
- Tsamados, M., Feltham, D. L., Schroeder, D., Flocco, D., Farrell, S. L., Kurtz, N., Laxon, S. L., and Bacon, S.: Impact of Variable Atmospheric and Oceanic Form Drag on Simulations of Arctic Sea Ice. *J. Phys. Oceanogr.*, 44(5), 1329–1353, doi:10.1175/JPO-D-13-0215.1, 2014.
- Uttal T., Curry J. A., McPhee, M. G., Perovich, D. K., Moritz, R. E., Maslanik, J. A., Guest, P. S., Stern, H. L., Moore, J. A., Turenne, R., Heiberg, A., Serreze, M. C., Wylie, D. P., Persson, P. O. G., Paulson, C. A., Halle, C., Morison, J. H., Wheeler, P. A., Makshtas, A., Welch, H., Shupe, M. D., Intrieri, J. M., Stamnes, K., Lindsey, R. W., Pinkel, R., Pegau, W. S., Stanton, T. P., and Grenfeld, T. C.: Surface Heat Budget of the Arctic Ocean. *Bull. Am. Meteorol. Soc.*, **83**: 255–275, doi:10.1175/1520-0477(2002)083<0255:SHBOTA>2.3.CO;2, 2002.
- Vancoppenolle, M., Bouillon, S., Fichefet, T., Goosse, H., Lecomte, O., Morales Maqueda, M. A. and Madec, G.: The Louvain-la-Neuve sea Ice Model Users Guide, 89 pp. Available: <http://www.elic.ucl.ac.be/repomodx/lim/>, 2012.
- Vihma, T.: Subgrid Parameterization of Surface Heat and Momentum Fluxes over Polar Oceans, *J. Geophys. Res.*, 100, 22625–22646, doi:10.1029/95JC02498, 1995.
- Wadhams, P., Squire, V. A., Goodman, D. J., Cowan, A. M., & Moore, S. C.: The attenuation rates of ocean waves in the marginal ice zone. *J. Geophys. Res. Oceans* (1978–2012), 93(C6), 6799–6818, doi:10.1029/JC093iC06p06799, 1988.
- Weiss, A. I., King, J., Lachlan-Cope, T., and Ladkin, R.: On the effective aerodynamic and scalar roughness length of Weddell Sea ice, *J. Geophys. Res.*, 116, D19119, doi:10.1029/2011JD015949, 2011.

972 Weiss, A. I., King, J. C., Lachlan-Cope, T. A., & Ladkin, R. S.: Albedo of the ice-covered Weddell  
973 and Bellingshausen Sea. *The Cryosphere Discuss.*, 5, 3259-3289, doi:10.5194/tcd-5-3259-  
974 2011, 2011.  
975

	$c_e$	$s$	$D_{min}$	$D_{max}$	$h_{min}$	$h_{max}$	$\beta$
L2012	0.3	0.5	8 m	300 m	0.286 m	0.534 m	1
CICE	<del>0.2</del>	0.18	8 m	300 m	0.286 m	0.534 m	1
<a href="#">E15E2016A</a>	0.17	0.5	8 m	300 m	0.286 m	0.534 m	1
<a href="#">E15E2016B</a>	0.1	0.5	8 m	300 m	0.286 m	0.534 m	0.2

**Table 1** Parameter settings for the form drag component of the L2012 scheme (Lüpkes et al. 2012): as recommended in L2012, as used in CICE (Tsamados et al. 2014) and as recommended here ([E15E2016A](#) and [E15E2016B](#)). Grey text indicates no change from the original L2012 value.

Date	Flight no.	No. legs	No. runs	No. ‘good’ $\tau$ runs	Mean altitude (m AMSL)	Mean wind speed ( $\text{m s}^{-1}$ )	Flight location
21-Mar	B760	1	18	17	79	7.8	Barents Sea
22-Mar	B761	1	7	7	38	7.4	Barents Sea
23-Mar	181	6	40	37	36	8.3	Barents Sea
25-Mar	182	6	37	33	39	7.2	Fram Strait
26-Mar	183	7	36	34	29	7.2	Fram Strait
29-Mar	184	6	30	29	33	6.9	Fram Strait
30-Mar	B765	1	9	9	41	8.9	Barents Sea
31-Mar	185	8	32	29	33	4.9	Barents Sea

**Table 2.** Summary of flights during the March 2013 ACCACIA field campaign. Flight numbers preceded by the letter ‘B’ use the FAAM BAE146; the other flights use the MASIN Twin Otter.

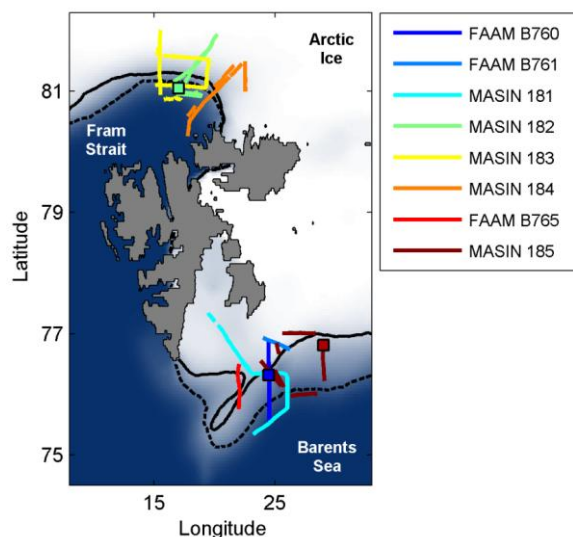


**Figure 1.** Map of Svalbard (landmass in grey) and the surrounding ocean and sea ice. The blue-white shading conveys the mean sea ice fraction from the satellite-derived Operational Sea Surface and Sea Ice Analysis (OSTIA) for the March 2013 field campaign, while contours at 0.5 ice fraction illustrated the maximum (dashed black) and minimum (solid black) extents. The relevant flight legs are plotted in colour and listed in chronological order in the legend. Coloured squares show the locations of the images shown in Figures 5 and 6.

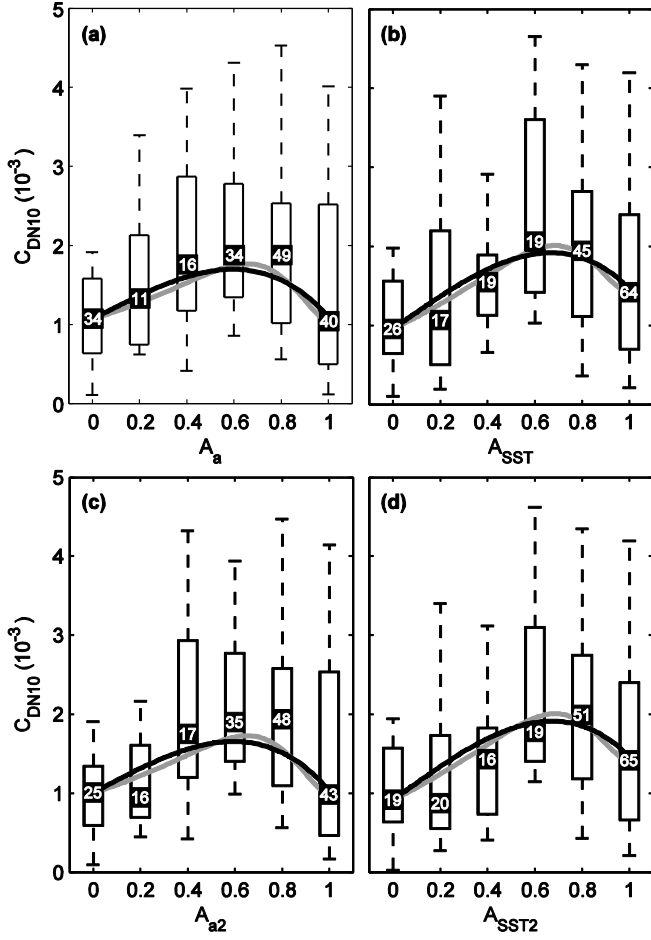


**Figure 2.**  $C_{DN10}$  as a function of ice fraction  $A$ : (a)  $A_a$  (from albedo); (b)  $A_{SST}$  (from sea surface temperature with a *no ice transition* at  $-3.4$  °C); (c)  $A_{a2}$  (from albedo with alternative tie points); and (d)  $A_{SST2}$  (from SST with a *no ice transition* at  $-1.8$  °C). Observational data are arranged in ice fraction bins of interval 0.2. Box and whisker plots show the median (black square), interquartile range (boxes) and 9<sup>th</sup> and 91<sup>st</sup> percentiles (whiskers) within each bin. The number of data points within each bin is indicated at the bin-median level. The L2012 scheme is illustrated by curves anchored at our observed values for  $A = 0$  and  $A = 1$ , using parameter settings [E15E2016A](#) (black curve) and [E15E2016B](#) (grey curve) in Table 1.

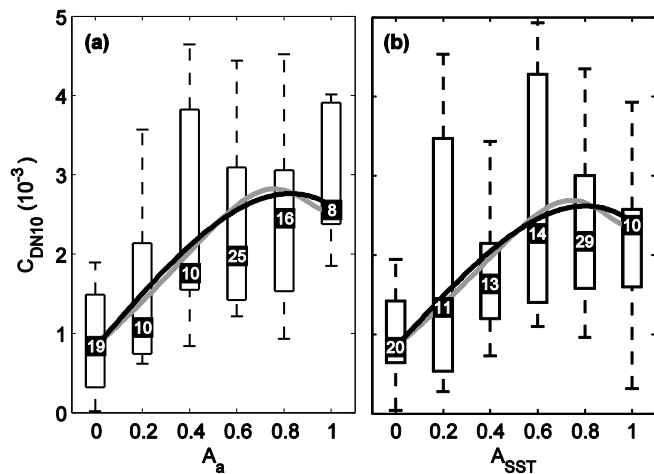


**Figure 3.** As in Fig. 2, but for Barents Sea flights only (see Table 2 for details of flights).

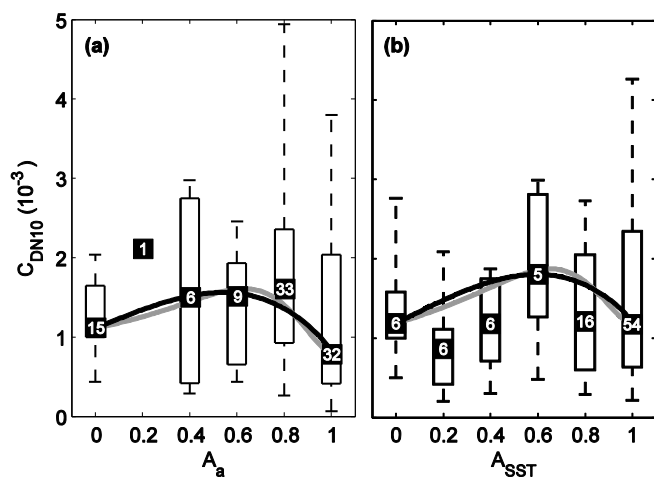
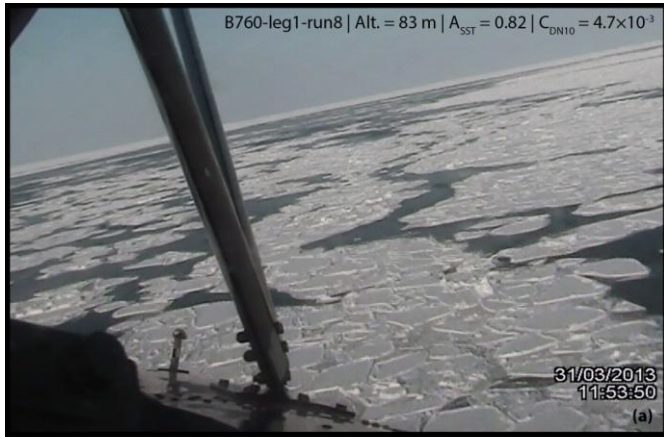


**Figure 4.** As in Fig. 2, but for Fram Strait flights only (see Table 2 for details of flights).

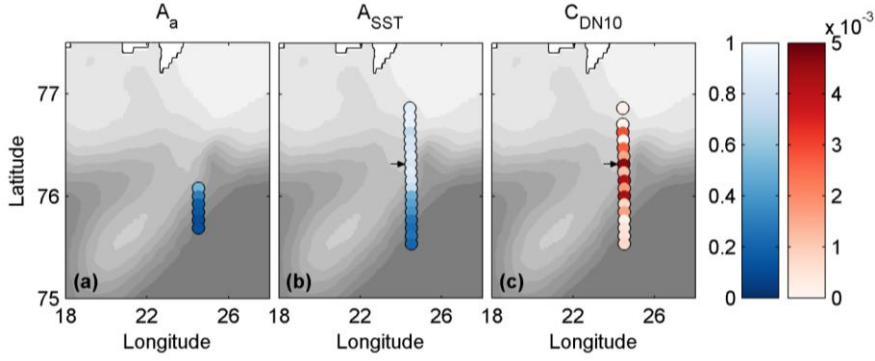




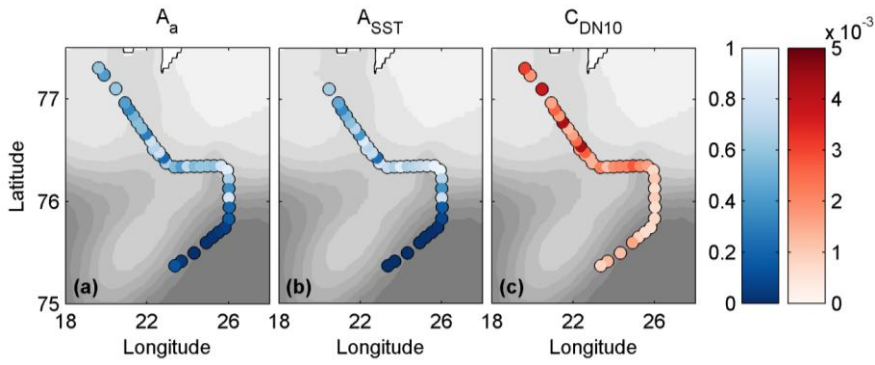
1009  
1010 **Figure 5.** a) Photograph taken from the FAAM aircraft during the Flight B760 *flux-run* marked  
1011 with an arrow in Fig. 7; and b) still from video recorded from the MASIN aircraft during Flight  
1012 185. The image locations are marked on Fig. 1.



1013  
1014 **Figure 6.** Photograph taken from the MASIN aircraft between legs 3 and 4 during Flight 182 at an  
1015 altitude of ~100 m. The location is marked on Fig. 1.  
1016



1017  
 1018 **Figure 7** Spatial maps of ice fraction a)  $A_a$ , b)  $A_{SST}$  and drag coefficient c)  $C_{DN10}$  for all *flux-runs*  
 1019 during FAAM Flight B760. The background grey-scale shading is OSTIA sea ice concentration  
 1020 (lighter shades indicating higher ice concentrations).



1021  
 1022 **Figure 8** Spatial maps of ice fraction a)  $A_a$ , b)  $A_{SST}$  and drag coefficient c)  $C_{DN10}$  for all *flux-runs*  
 1023 during MASIN Flight 181, as Fig. 7.

1024

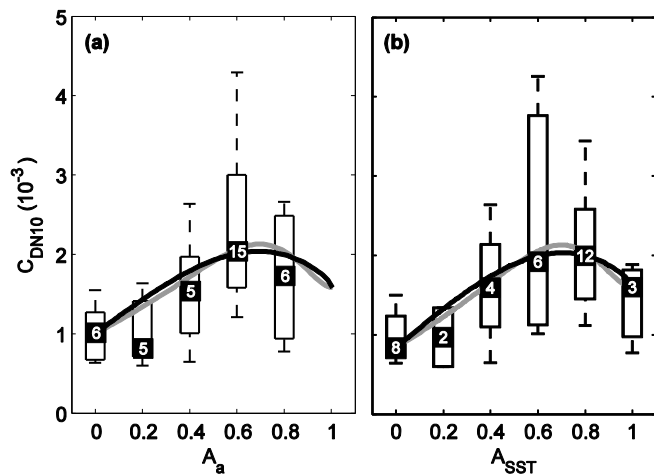
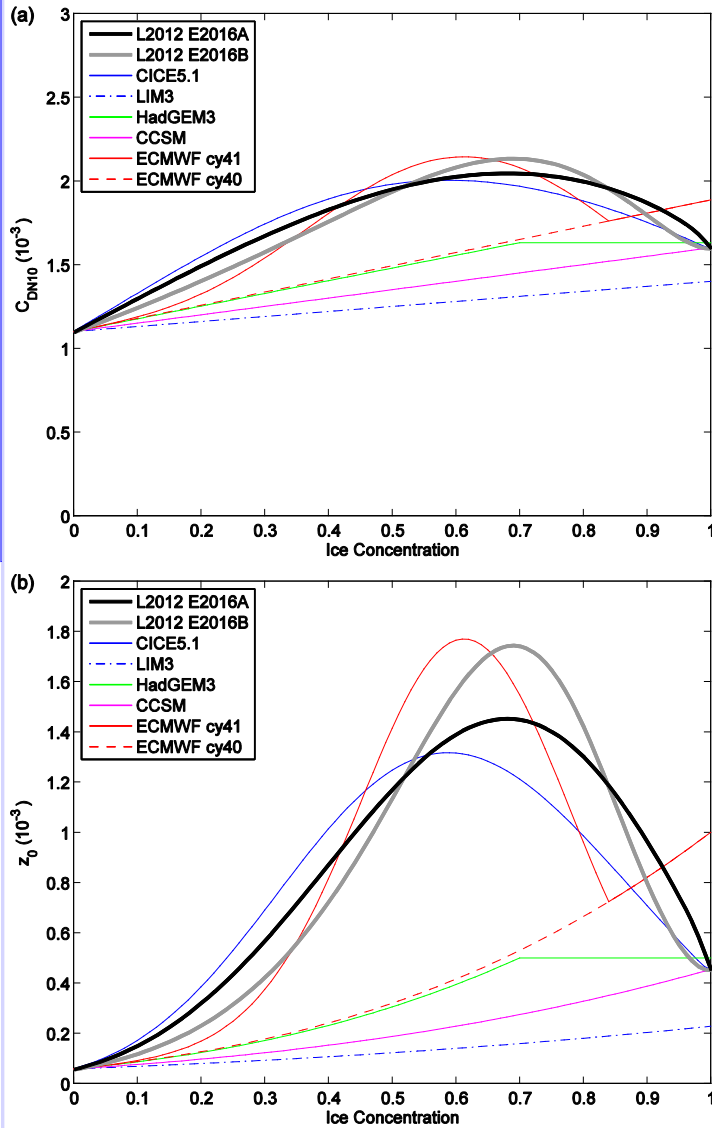
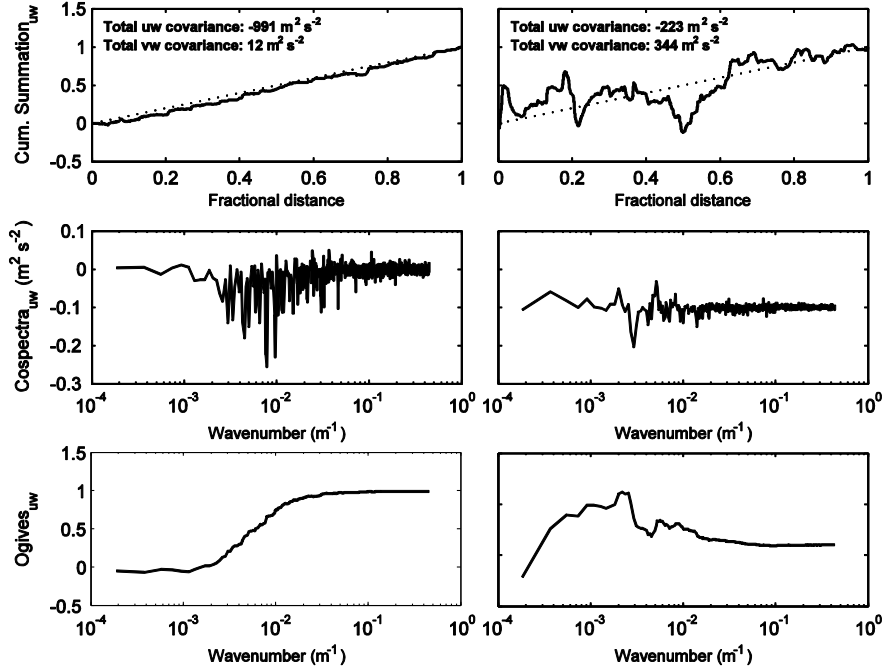


**Figure 9.** As in Fig. 2, but for flight 181 only (see Table 2 for flight details).

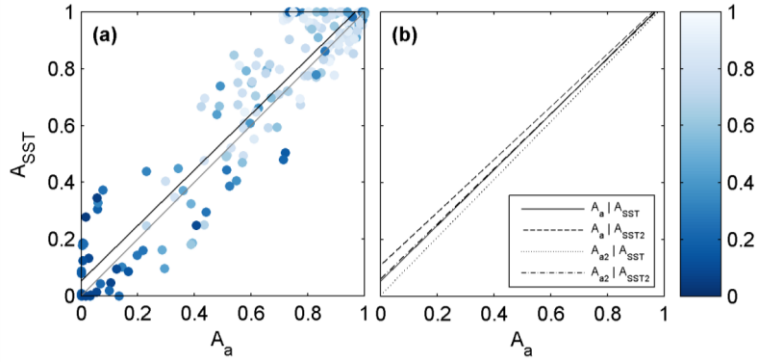


**Comment [a1]:** Note new version of this figure (with corrected CICE5.1 line following discovery of the error in Tsamados et al. (2014), and addition of panel b) showing same as panel b) but for effective roughness length)

**Figure 10** a) Effective sea-ice drag coefficients and b) derived effective roughness length as a function of ice concentration. Parameterizations shown are: Lüpkes et al. (2012) with settings as recommended here, namely L2012 E2016A with  $c_e = 0.17$  and  $\beta = 1$  (black), and L2012 E2016B with  $c_e = 0.1$  and  $\beta = 0.2$  (grey); the default L2012 settings used in CICE5.1 (blue) as described in Tsamados et al. (2014); the LIM3 interpolation (blue dashed-dotted); the HadGEM3 default used in the Met Office Unified Model (green); the CCSM (and CAM5) interpolation (magenta); the ECMWF cycle 41 function (red) and the previous ECMWF cycle 40 interpolation (red dashed). See Table 1 for other L2012 settings.



**Figure A1.** Quality control diagnostics for momentum flux ( $u'w'$ ). Left column shows a 'good' run (flight 181, leg 2, run 7); right column shows a 'bad' run (flight 181, leg 5, run 11). The rows show (top) the cumulative summation of  $u'w'$  versus distance along the run; (middle) the frequency weighted cospectra; and (bottom) the ogives (integrated cospectra) both as a function of wavenumber. The cumulative summation is normalised by the total covariance and the ogives by the total co-spectra.



1046  
 1047 **Figure A2.** Ice fraction calculated from aircraft observations using the surface temperature method  
 1048 ( $A_{SST}$ ) plotted against that using the albedo method ( $A_a$ ). (a) Data points for every run (dots) and  
 1049 linear regression (black line) are shown, using the default criteria for both methods ( $a_{A \rightarrow 0} = 0.15$   
 1050 and  $SST_{A \rightarrow 0} = -3.4$  °C). Dots are coloured according to the OSTIA satellite-derived ice fraction, and  
 1051 the one-to-one line (grey) is shown. (b) Linear regressions of all combinations of observation-  
 1052 derived  $A_a$  and  $A_{SST}$ .